Characterising radiation-belt energetic electron precipitation spectra: a comparison of quasi-linear diffusion theory with in-situ measurements

J. A. Reidy[1], R. B. Horne[1], S. A. Glauert[1], M. A. Clilverd[1], N. P. Meredith[1], C. J. Rodger, [2]J. P. Ross[1], J. Wong[1]

[1]British Antarctic Survey, Natural Environment Research Council, Cambridge, UK
[2]Department of Physics, University of Otago, Dunedin, New Zealand

Key Points:

- Decreasing the cold plasma density increases calculated electron precipitation at the higher energies.
- Calculated precipitation for a low Earth orbiting detector is weakly dependent on the source spectrum.
- RBSP derived diffusion coefficients provide more diffusion for precipitating particles than those derived from a larger wave database.

Corresponding author: Jade Reidy, `jadeid70@bas.ac.uk`

Abstract

High energy electron precipitation from the Earth's radiation belts is important for loss from the radiation belts and atmospheric chemistry. We follow up investigations presented in Reidy et al. (2021) where precipitating flux is calculated inside the field of view of the POES T0 detector using quasi-linear theory and pitch angle diffusion coefficients ($D_{\alpha\alpha}$) from the British Antarctic Survey (BAS). These results showed good agreements at >30 keV for L* >5 on the dawnside but the flux were too low at higher energies. We have investigated the effect of changing parameters in the calculation of the precipitating flux to improve the results for the higher energies using comparisons of in-situ flux and cold plasma measurements from GOES-15 and RBSP. We find that the strength of the diffusion coefficients rather than the shape of the source spectrum has the biggest effect on the calculated precipitation. In particular we find decreasing the cold plasma density used in the calculation of $D_{\alpha\alpha}$ increases the diffusion and hence the precipitation at the loss cone for the higher energies, improving our results. The method of calculating $D_{\alpha\alpha}$ is also examined, comparing co-located rather than averaged RBSP measurements. We find that the method itself has minimal effect but using RBSP derived $D_{\alpha\alpha}$ improved our results over using $D_{\alpha\alpha}$ calculated using the entire BAS wave data base; this is potentially due to better measurements of the cold plasma density from RBSP than the other spacecraft included in the BAS wave data base (e.g. THEMIS).

Plain Language Summary

High energy particles trapped in the Earth's radiation belt can enter the atmosphere, known as particle precipitation, and collide with atmospheric particles, which can change the atmospheric chemistry. This input into our atmosphere is key to understanding the effects of space weather on our climate system variability but is difficult to quantify. Reidy et al. (2021) calculated the precipitation that would be measured by a low-Earth orbiting satellite using wave-particle theory and diffusion coefficients from a radiation belt model. Diffusion coefficients describe the amount of diffusion of the trapped radiation belt particle population driven by different sources (e.g. chorus waves). Reidy et al. (2021) found good agreement between the calculated and measured precipitation for lower energy particles but found there was something missing for the higher energies. This paper investigates the impact of changing certain parameters within the calculations, finding the cold plasma density to be key in improving the results at higher energies.

1 Introduction

High energy electron precipitation plays a significant role within magnetospheric dynamics, both as a mechanism of loss from the Earth's radiation belts and by the impact on the atmospheric chemistry. Several attempts have been made to quantify this input, using particle measurements from low-orbiting spacecraft, such as POES (e.g. Rodger, Clilverd, et al. (2010); Nesse Tyssøy et al. (2016)) and from ground-based instrumentation (e.g Rodger, Clilverd, et al. (2010); Rodger et al. (2013)). There have also been attempts to quantify precipitation from radiation belt models (e.g Jordanova et al. (2016); Ferradas et al. (2019)).

Recently, Reidy et al. (2021) used wave-particle theory to calculate the precipitating flux that would be measured by the POES particle detector orientated towards local zenith (termed T0), these calculations required bounce averaged pitch angle diffusion coefficients and a source spectrum for the differential flux. Reidy et al. (2021) compared the calculated T0 flux to in-situ measurements from POES; these calculations showed good agreement on the dawnside for L* > 5 for the >30 keV electron channel, as expected from using an averaged wave-model to generate the diffusion coefficients for chorus waves.

However, these calculations significantly underestimated the >100 keV flux, by more than a factor of 10 in some MLT/L* sectors.

For the differential source spectrum, Reidy et al. (2021) fitted a kappa distribution, assuming a spectral index of $\kappa = 5$, to the integral flux measurements from the POES telescope aligned perpendicular to T0 (termed T90), making sure the telescopes field of view was outside the loss cone and hence measuring trapped (or quasi-trapped) particles (see Appendix A of Rodger, Carson, et al. (2010)). A kappa distribution was first shown to be effective at modelling the particle distributions in the radiation belts by Summers and Thorne (1991) and has subsequently been used in several studies to represent the differential flux spectrum (e.g. Li et al. (2013) and Glauert et al. (2018)). Whittaker et al. (2013) found using DEMETER data that a spectral index of κ >2 worked well for fitting the distributions, with lower values of κ providing a harder spectrum.Whittaker et al. (2013) also applied power-law and exponential fits to the DEMETER electron spectra, finding a power-law spectral gradient to consistently provide the best fit. Using Van Allen Probes data during 2017, Zhao et al. (2019) found an exponential spectrum fit best outside the plasmasphere, with a power law mostly occurring during injections at high L*, whilst flux inside the plasmasphere was dominated by bump-on-tail distribution due to interactions with Hiss waves. The effect of these different types of spectral fit (i.e. power-law and exponential), as well as the impact of lowering the spectral index κ in the kappa-fit, on the calculated precipitation from Reidy et al. (2021) will be investigated in this paper.

Most radiation belt models, such as the British Antarctic Survey Radiation Belt model (BAS-RBM, Glauert et al. (2014)), solve a diffusion equation to quantify the evolution of flux within the radiation belts; wave-particle interactions are incorporated in these equations by diffusion coefficients. Diffusion coefficients can be calculated using statistical wave models, giving average diffusion coefficients based on averaged wave data for different geomagnetic activity levels (e.g Glauert and Horne (2005)) or from in-situ data giving event specific diffusion coefficients (e.g. Ripoll et al. (2019)). One of the key variables in diffusion coefficient calculations is the cold plasma density, which can alter the electron energy and pitch angles at which resonant interactions occur. Allison et al. (2021) found, using Radiation Belt Storm Probe (RBSP) in-situ waves and flux measurements, that decreases in the electron plasma density results in enhancements of the diffusion coefficients (both in energy and pitch angle) across all energy ranges. Allison et al. (2021) show that during extreme depletion's of the plasma density, energy diffusion due to chorus can be sufficiently high to accelerate electrons to >7 MeV energies. Allison et al. (2021) also note a decrease in density would increase pitch angle diffusion near the loss cone, thereby also increasing the loss from the radiation belts.

The method used to calculate diffusion coefficients has recently been examined; Watt et al. (2019) found very different values of diffusion coefficients, calculated with the same data sets, depending whether they were calculated from averaged values or if they were calculated using co-located measurements of the wave spectra and f_{pe}/f_{ce} and then averaged. Ross et al. (2020) re-calculated EMIC diffusion coefficients using co-located wave measurements rather than the averaged values and found better agreement when using them in a radiation belt model (BAS-RBM) compared with RBSP data. Similarly, Wong et al. (2022) found improvements for magnetosonic waves. This new method of calculating the diffusion coefficients with co-located data captures more variability of the system, allowing better representation of the extreme cases. Both Watt et al. (2019) and Ross et al. (2020) suggest other diffusion coefficients, such as that for chorus, should be re-calculated using similar techniques.

In this study we separately investigate the impact of the source spectrum, as well as two forms of variability within the diffusion coefficients, on the calculated precipitation using the same methods as in Reidy et al. (2021). In Section 2 we outline the instrumentation and methods used to evaluate the precipitation. In Section 3.1, we compare the differential flux spectrum derived from POES T90 measurements (used as the source spectrum for calculating precipitation in Reidy et al. (2021)), with in-situ differential flux measurements made by GOES-15, when GOES-15 and the POES spacecraft were in the same L* and Magnetic Local Time (MLT) sector during March 2013. We then investigate the impact of changing the shape of the source spectrum on the calculated precipitation. In Section 3.2, we investigate the impact of the cold plasma density on the amount of pitch angle diffusion at the loss cone, first by comparing the modelled f_{pe}/f_{ce} with in-situ measurements from RBSP-A during November 2012 (a time when the RBSP orbit was at high L-shell on the dawnside, between 06-08 MLT) and then by re-calculating the chorus diffusion coefficients with f_{pe}/f_{ce} multiplied and divided by two. Lastly, in Section 3.3 we re-calculate the chorus diffusion coefficients using RBSP data, firstly with averaged measurements and then using co-located measurements in a similar way to Ross et al. (2021). We present discussions and conclusions of these investigations in Sections 4 and 5 respectively.

2 Instrumentation and method

2.1 Polar Orbiting Environmental Satellite (POES)

The POES constellation are low Earth orbiting satellites (800–850 km altitude), in Sun-synchronous orbits. We are using data from the Medium Energy Proton and Electron Detectors (MEPED) instrument, part of the Space Environment Monitor (SEM-2) package. MEPED has two electron solid state detectors, one centered 9° off local zenith (T0) and the other perpendicular to this (T90). These instruments provide integral flux measurements of the electrons between 30 and 2500 keV in three channels (>30, >100, and >300 keV) (Evans & Greer, 2004). We have combined data from the POES spacecraft NOAA15 to 19. These data have been corrected from proton contamination using the bow tie method described in Lam et al. (2010). We average all observations in 0.5 L* (calculated using the Olson Pfitzer Quiet model (Olson & Pfitzer, 1977)) for direct comparison with the diffusion coefficients from the BAS wave model. As we are using data from multiple POES satellites (NOAA15-19) we have data covering a wide range of magnetic local time sectors but predominately focus between 9-12 MLT for this paper. For reference the local times of each satellite, for the ascending node, are given in Table 2 of Sandanger et al. (2015).

During our calculations of the electron precipitation it is important to know when the T0/T90 detector fields of view (30° wide) are inside/outside the equatorial loss cone (the pitch angle of the loss cone when mapped along the magnetic field to the equator). To do this we project the field of view of the instruments to the equator, using the Olson and Pfitzer (1977) magnetic model.

Figure 1 shows the integral flux measurements made by POES, for three L* bins of interest between 00-12 MLT during 26-30 March 2013; to show the general trend in the data we have used a line plot however, we note these data are not continuous but rather made from several spacecraft as outlined above. The Kp is shown in the bottom panel. We have used a noise threshold of 1000 $cm^{-2}sr^{-1}s^{-1}$, which the precipitating flux measured by T0 (solid line) is generally below during low Kp. Therefore, when we calculate the precipitation for this event we are typically looking during moderate to high activity levels. Furthermore, the >300 keV electron flux (not shown) is not above this noise level and hence not considered in this paper. We also note that the modelled location of the plasmapause (blue line in the bottom panel, calculated as described in Meredith et al. (2018)) doesn't go above L* = 5 during this event.

There has been some question about the validity of the T0 measurements; Selesnick et al. (2020) suggest the T0 telescope predominately measures stably trapped or quasi trapped flux in the drift loss cone rather than precipitating flux in the bounce loss cone.

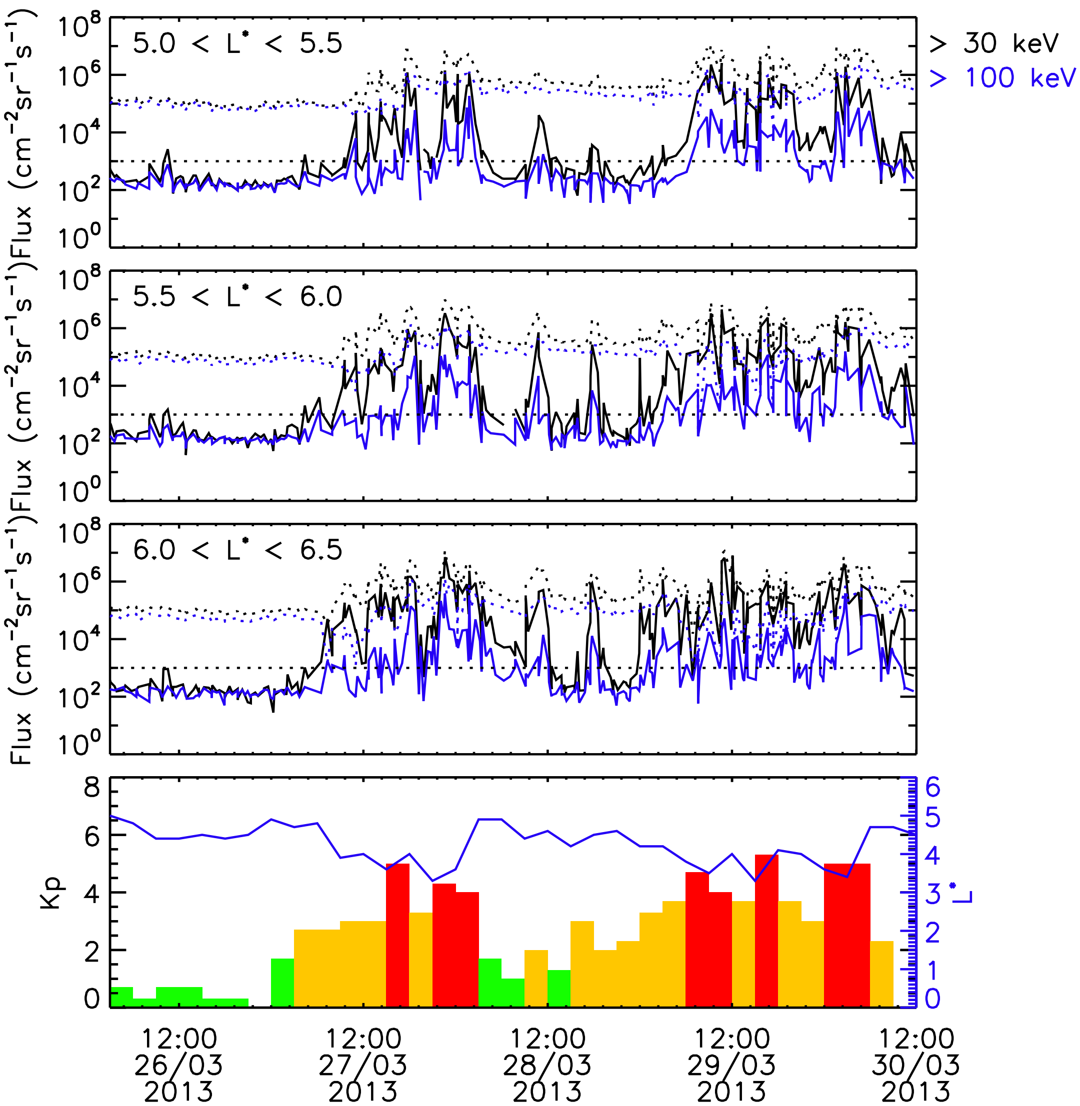

Figure 1. Integral flux measurements made by T0 (solid lines) and T90 (dotted lines) for >30 keV (black) and >100 keV (blue) electrons from the POES satellites averaged in 0.5 L* for 5 < L* < 5.5 (top panel), 5.5 <L* < 6 (second panel), 6 < L* < 6.5 (third panel) between 26-30 March 2013. The bottom panel shows the Kp during this event and the blue line demonstrates the modelled location of the plasmapause (dependent on Kp and MLT) from the BAS wave model. The colour of Kp indicates the activity levels with low activity (0< Kp <2) shown in green, moderate activity (2< Kp < 4) in orange and high activity (Kp >4) indicated in red.

However, Rodger et al. (2022) point out that the T0 measurements have been cross-calibrated using multiple different independent data sets (one example being VLF/LF transmitters by Clilverd et al. (2010)) that do suggest T0 measures the precipitating flux. Furthermore, we have limited ourselves to measurements above a relatively high noise threshold (1000 $\text{cm}^{-2}\text{sr}^{-1}\text{s}^{-1}$, shown by dotted line in Figure 1), where the precipitation should dominate the T0 measurements.

2.2 Geostationary Operational Environmental Satellite (GOES)

We are using data from the MAGED (MAGnetospheric Electron Detector) instrument on board GOES-15, which provides the differential electron flux at five different energies (40 keV, 75 keV, 150 keV, 275 keV and 475 keV) and has nine telescopes with different look angles (Onsager et al., 1996). It is possible that the flux may vary with pitch angle but by using telescope 9 we are using the closest in pitch angle to T90. We note that the pitch angle for the telescope 9 of MEPED/GOES is changing depending on geomagnetic activity, since the intensity of the ambient geomagnetic field at GOES 15 is comparable to the magnitude of geomagnetic field variations, however during this interval the pitch angle is varying approximately between 15° and 10° between 26- 30 March 2013 (for reference, T90 has a pitch angle of 3° at GOES L-shells during this interval).

2.3 Radiation Belt Storm Probe (RBSP-A)

We have obtained data from one of the twin Van Allen Probes (RBSP), Radiation Belt Storm Probes A (RBSP-A) Electric and Magnetic Field Instrument Suite and Integrated Science (EMFISIS) (Kletzing et al., 2013). The Van Allen Probes have a 9 hour orbit near the magnetic equator with a ∼10° inclination and a perigee of ~ 1.1 R_E (Mauk et al., 2013). EMFISIS measures magnetic and electric fields between approximately 10 Hz up to 400 kHz, providing a comprehensive set of magnetospheric wave properties, which are later used to calculate chorus diffusion coefficients. The electron plasma frequency, f_{pe}, is provided as a Level 4 data product and is derived either from the upper hybrid frequency (when visible) or by the lower frequency continuum radiation (Kurth et al., 2015a). The electron gyrofrequency, f_{ce}, is found using measurements of the local magnetic field made by the 1s fluxgate magnetometer.

We have used data from November 2012, when RBSP were orbiting at high L* on the dawnside, to compare to modelled values of the f_{pe}/f_{ce} used to calculate chorus diffusion coefficients. We have also used 7 years of RBSP wave and cold plasma measurements between November 2012 to October 2019, to calculate chorus diffusion coefficients using two different methods, as described later.

2.4 Quasi-linear theory

As in Reidy et al. (2021), we use the steady state solution to a Fokker Planck equation for pitch angle diffusion from Kennel and Petschek (1966) to calculate the precipitating flux.

Where

$$J_{eq}(E, \alpha_{eq}) = N\ S(E)\ D_{\alpha\alpha}(\alpha_0)^{-1} \left[h(\alpha_0) + \ln\left(\frac{\sin\alpha_{eq}}{\sin\alpha_0}\right)\right], \tag{1}$$

outside the loss cone ($\alpha_0 \leq \alpha_{eq} \leq \frac{\pi}{2}$),

$$J_{eq}(E, \alpha_{eq}) = N\ S(E)\ D_{\alpha\alpha}(\alpha_0)^{-1}\ h(\alpha_{eq}), \tag{2}$$

inside the loss cone ($\alpha_{eq} \le \alpha_0$) and

$$h(\alpha_{eq}) \equiv \frac{\sqrt{D_{\alpha\alpha}(\alpha_0)\tau}}{\alpha_0}\left[\frac{I_0\left(\frac{\alpha_{eq}}{\sqrt{D_{\alpha\alpha}(\alpha_0)\tau}}\right)}{I_1\left(\frac{\alpha_0}{\sqrt{D_{\alpha\alpha}(\alpha_0)\tau}}\right)}\right]. \quad (3)$$

$J_{eq}(E, \alpha_{eq})$ is the equatorial flux distribution for electrons, $D_{\alpha\alpha}(\alpha_0)$ are bounce-averaged pitch angle diffusion coefficients, α_{eq} are the equatorial pitch angles, E is the energy, τ the escape time (assumed to be a quarter of a bounce period), I_0 and I_1 are modified Bessel functions and N is a normalisation factor, $S(E)$ is the source of particles (N and $S(E)$ are defined based on the source spectrum).

For $D_{\alpha\alpha}(\alpha_0)$, we combine contributions from chorus and Coulomb collisions from the BAS-RBM wave model as in Reidy et al. (2021). These waves are used to calculate the $D_{\alpha\alpha}(\alpha_0)$ using the PADIE (Pitch Angle and Energy Diffusion of Ions and Electrons) code, which calculates fully relativistic pitch angel, energy and mixed diffusion coefficients for resonant wave particle interactions as described in Glauert and Horne (2005). The BAS wave model is based on measurements from multiple different satellites which are binned by location and geomagnetic activity e.g. the chorus waves described in Meredith et al. (2020). The effects of hiss waves are not included, as we are looking at L^* outside the plasmasphere, as assumed by our modelled plasmapause location shown in the bottom panel of Figure 1. Diffusion due to EMIC waves are included but are negligible at the energies we consider. At each time of consideration, the $D_{\alpha\alpha}(\alpha_0)$ is evaluated at the edge of the loss cone based on the L^*/MLT location of the spacecraft and the current geomagnetic activity level. The calculation and specifics of these diffusion coefficients will be discussed in more detail in Section 3.3.

3 Results

3.1 The impact of the shape of the source spectrum

Figure 2 shows the MLT location of the GOES-15 and POES satellites between 26-30 March 2013. The POES flux data are a combination from NOAA-16, -17 and -19 (which have been individually averaged over 2 minutes and 0.5 L^* before being combined), between $6 < L^* < 6.5$ for consistency with the GOES flux data at geostationary orbit. The GOES flux data are at 2 minute resolution. To find a conjunction between POES and GOES during this time, we require the spacecraft to be within 0.1 hours of MLT of each other and within an hour of UT. Furthermore, before we use the POES data to calculate the precipitation, we require the entire T0 field of view to be within the loss cone, the entire T90 field to be outside the loss cone, the flux measured by the >30 keV channel to be greater than the flux measured by the >100 keV channel and the flux measured by the >100 keV channel to be greater than the flux measured by the >300 keV channel. We also imposed a noise threshold of 1000 cm^{-2} sr^{-1} s^{-1} and do not use any measurements when POES is within the longitudinal range of the South Atlantic Magnetic Anomaly. We find three conjunctions that meet this criteria that will be discussed below, shown by red asterisks in Figure 2.

Figures 3a, b and c show the differential flux measured by GOES telescope 9 at the three conjugate times in black asterisks. We have then fitted a power law (black dashed line) and an exponential (black dot-dashed line) to the GOES data at each time. It can be seen for the first two times (a and b), that the data shows better agreement with the exponential fit whereas the third time (c), the data fits better to the power law fit. This is similar to that previously found by Clilverd et al. (2010) and Whittaker et al. (2013). In Figures 3a, b and c, we also show the source spectra fitted from the POES T90 measurement assuming different spectral shapes: two kappa distributions with $\kappa = 5$ (as used in Reidy et al. (2021) (solid line)) and $\kappa = 2$ (dotted line), then an exponential fit (dot-

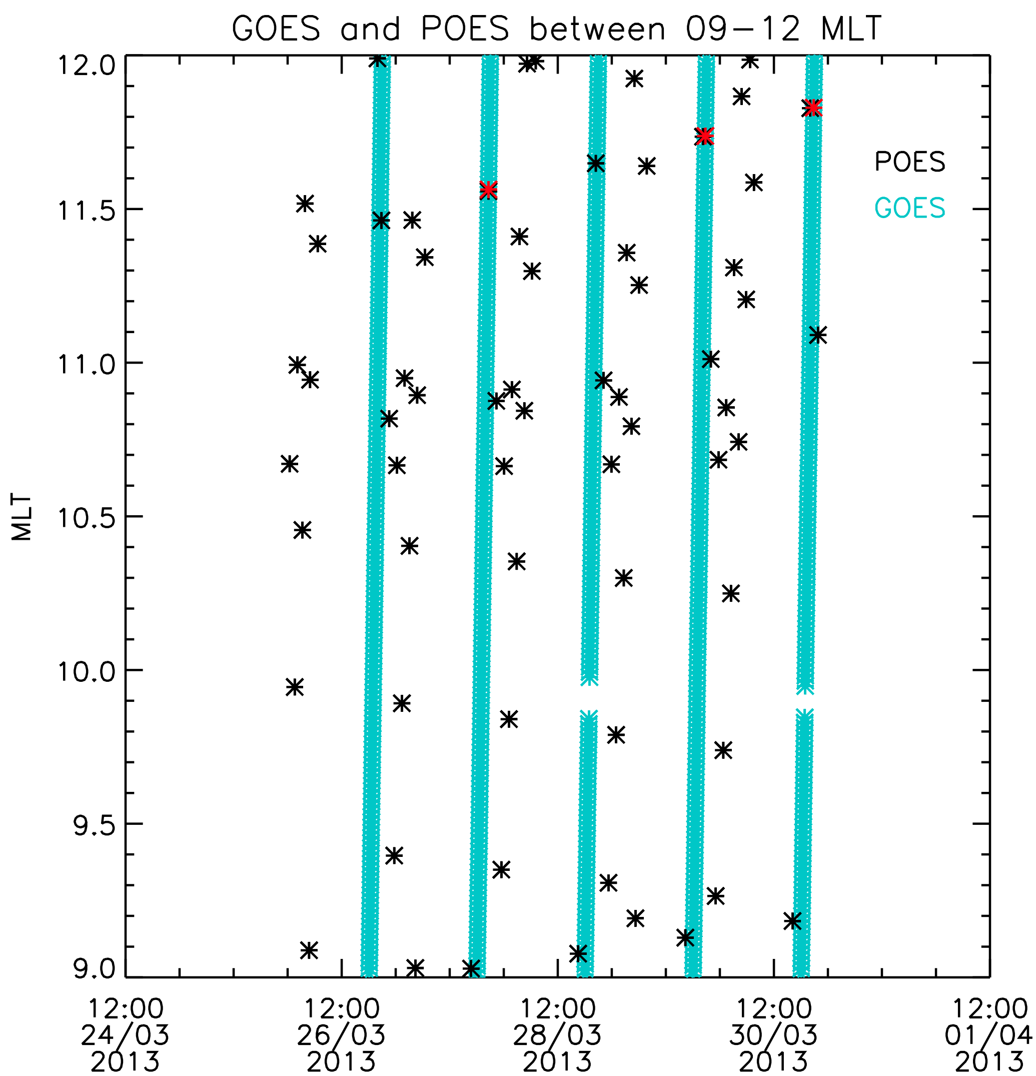

Figure 2. Showing the data from POES and GOES as a function of MLT during event, shown in black and blue respectively. The red asterisks are times when the criteria for a conjugate observation has been met.

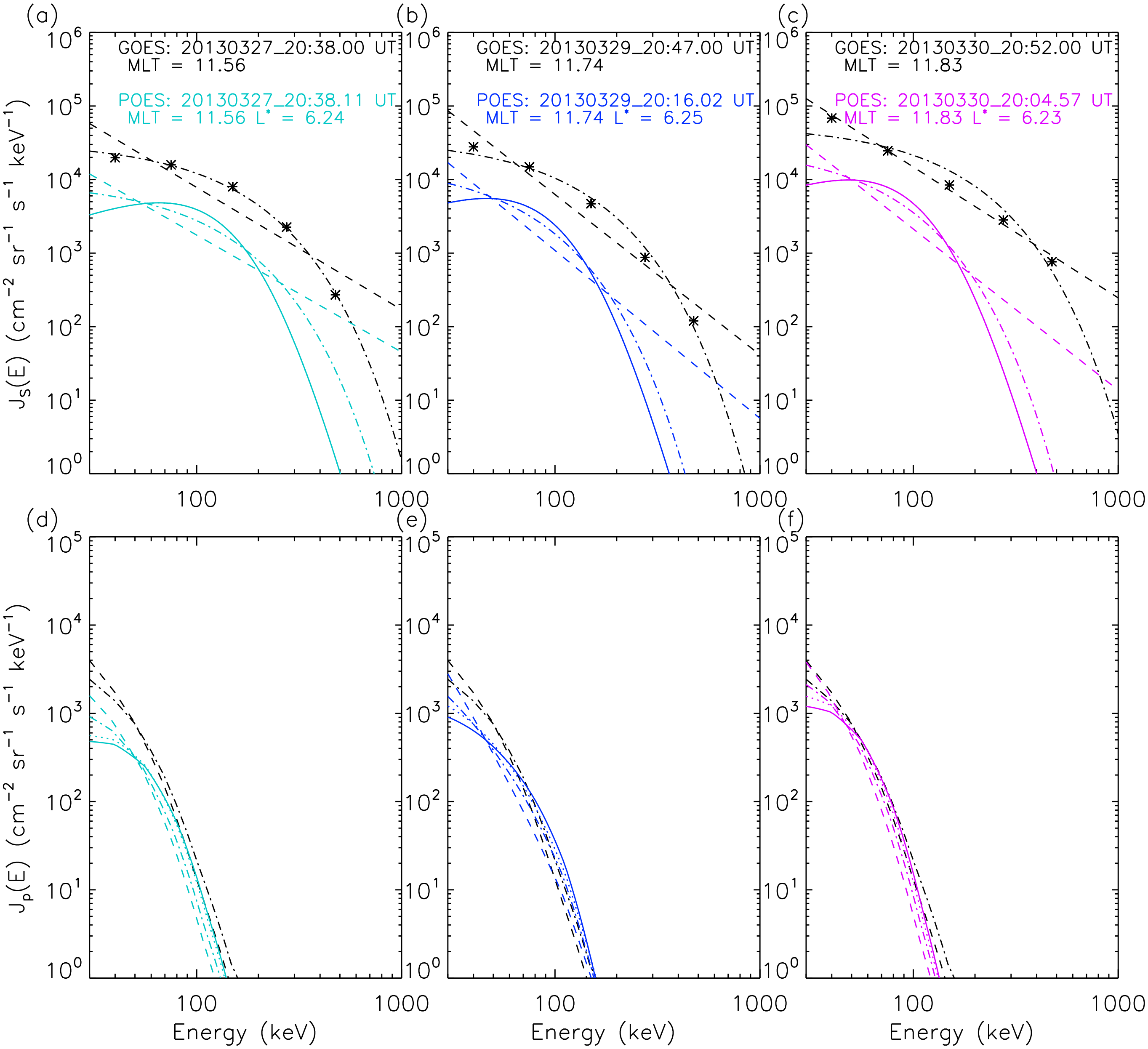

Figure 3. Figures a, b and c show the different fitted differential source spectra for the three conjugate times. The in-situ GOES-15 data are shown by black asterisks, fitted exponential and power law source spectra are shown in black dot-dashed and dashed lines respectively. The POES T90 data fitted to an exponential (dot-dashed), power law (dashed), $\kappa = 5$ (solid line) and $\kappa = 2$ (dotted line) are also shown in different colours for the three times. The corresponding calculated T0 precipitating spectra for each source spectra are shown in Figures d, e and f. The time and MLT of the GOES and POES measurements for each conjunction are provided in the top panel where the date format is YYYYMMDD_HH:mm:ss UT.

dashed) line and a power law fit (dashed lines). We note that the $\kappa = 5$ fit gives the lowest flux measurements at 30 keV and at the higher energies but there is a 'turn over' in the middle energies where the $\kappa = 5$ fit has the highest flux, the $\kappa = 2$ fit is similar but provides a higher spectrum, as expected, with the exponential fit almost between the two; the power law fit has the highest flux at the higher energies.

At each conjunction time, we have calculated the corresponding precipitating spectra using equations 1-3 for each of the six source spectral shapes, shown in Figs 3d-f. Table 1 gives the ratio of the calculated to measured T0 precipitating flux at each time for the >30 keV and >100 keV channels for each of the source terms. We note for the POES fitted source terms, there is very little difference across the four shapes of the source spectra, with a power law doing best for the >30 keV channel at times 1 and 2 but worse for time 3, which coincidentally was the time that the GOES data were best fit by a power law. The GOES power law source term however, does a good job at reproducing the measured >100 keV T0 flux at time 3 (with a ratio of 0.87) but is drastically overproducing the >30 keV flux (ratio of 5.58). The precipitating flux calculated using the GOES source terms is generally higher than that calculated from POES, this is likely due to the GOES flux measurements being at a higher pitch angle than POES and hence providing a larger magnitude of the source flux. Overall from this table, there is no clear fitted spectra representation of the source spectra that is doing significantly better than the rest for both integral channels for all three times. Furthermore, as seen in figures 3d, e and f, there is very little difference between the different calculated precipitation spectra for the different source spectral shapes, the biggest difference can be seen at 30 keV, where the GOES-based spectra have the highest flux, followed by the POES power law fit. The lowest precipitating flux at 30 keV is from the $\kappa = 5$ fit, which we note was used in Reidy et al. (2021) for their precipitation calculations. The precipitating flux for all the different source spectra falls off exponentially around 200 keV, showing that the hardness of the spectrum is making very little difference at the higher energies.

	Time 1		Time 2		Time 3	
	>30 keV	>100 keV	>30 keV	>100 keV	>30 keV	>100 keV
GOES PL	1.38	0.09	2.43	1.36	5.58	0.87
GOES exp	1.15	0.16	1.88	2.68	3.92	1.45
κ=2	0.43	0.07	0.86	0.55	1.93	0.33
κ=5	0.40	0.07	0.78	0.66	1.73	0.39
exp.	0.49	0.06	0.86	0.56	1.98	0.32
P.L.	0.59	0.04	1.00	0.35	2.39	0.20

Table 1. Ratio of calculated to measured T0 flux from >30 and >100 keV channels for different source spectra at the three conjunction times.

To investigate why the precipitating flux is dropping off so rapidly at the higher energies, we looked back at the solution to the Fokker-Planck diffusion equation from Kennel and Petschek (1966) given by Equations 1-3. Figure 4 shows the pitch angle distribution for 30 keV, 100 keV, 250 keV and 500 keV electrons using a POES power law source term (solid line) and also the POES exponential fit (dashed line) at the time of the first POES-GOES conjunction (previously termed Time 1 where, 11< MLT <12, 6< $L^* \leq 6$, 0< Kp <2). The angle of the loss cone is indicated by the vertical dotted line and fields of view of the POES T0 and T90 are shown by grey shaded regions. As discussed in Theodoridis and Paolini (1967), the shape of the flux within the loss cone is determined by the strength of the diffusion coefficient; the higher the diffusion rate, the flatter the flux in the loss cone becomes, up to the strong diffusion limit (as shown in Figure 4 of Reidy et al. (2021)). The diffusion coefficient from the BAS model used in the flux calculation for each energy level is indicated on Figure 4, which decrease with increasing energy, as expected

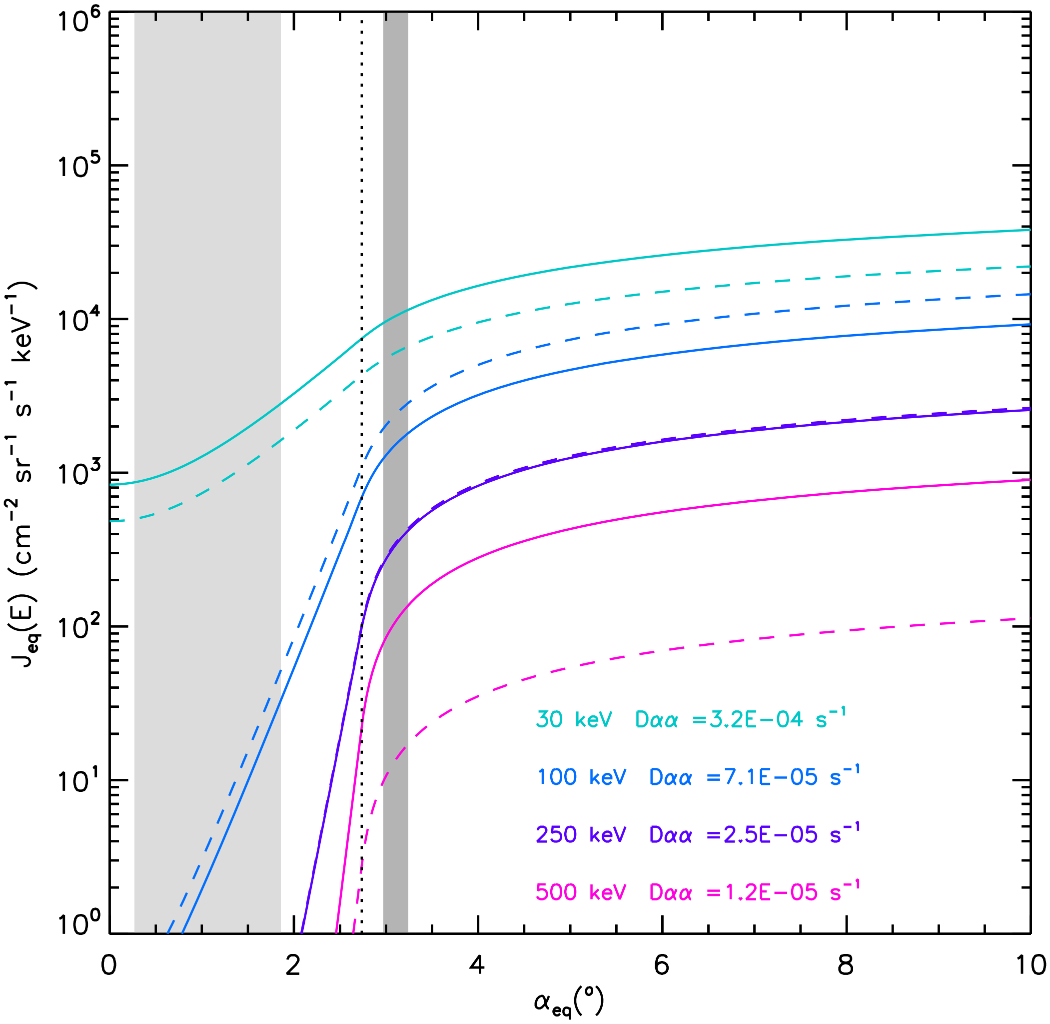

Figure 4. Figure showing the differential flux calculated from Kennel and Petschek (1966) solution for 30 keV (cyan), 100 keV (blue), 250 keV (purple) and 500 keV (pink) electrons with a source spectrum fitted to a power law (solid line) and an exponential (dashed line) based on POES T90 at 20:38.11 UT on 27 March 2013 (i.e. Time 1 in Table 1) The field of view of POES T0 and T90 projected to the equator are indicated by the light and dark grey shaded boxes respectively.

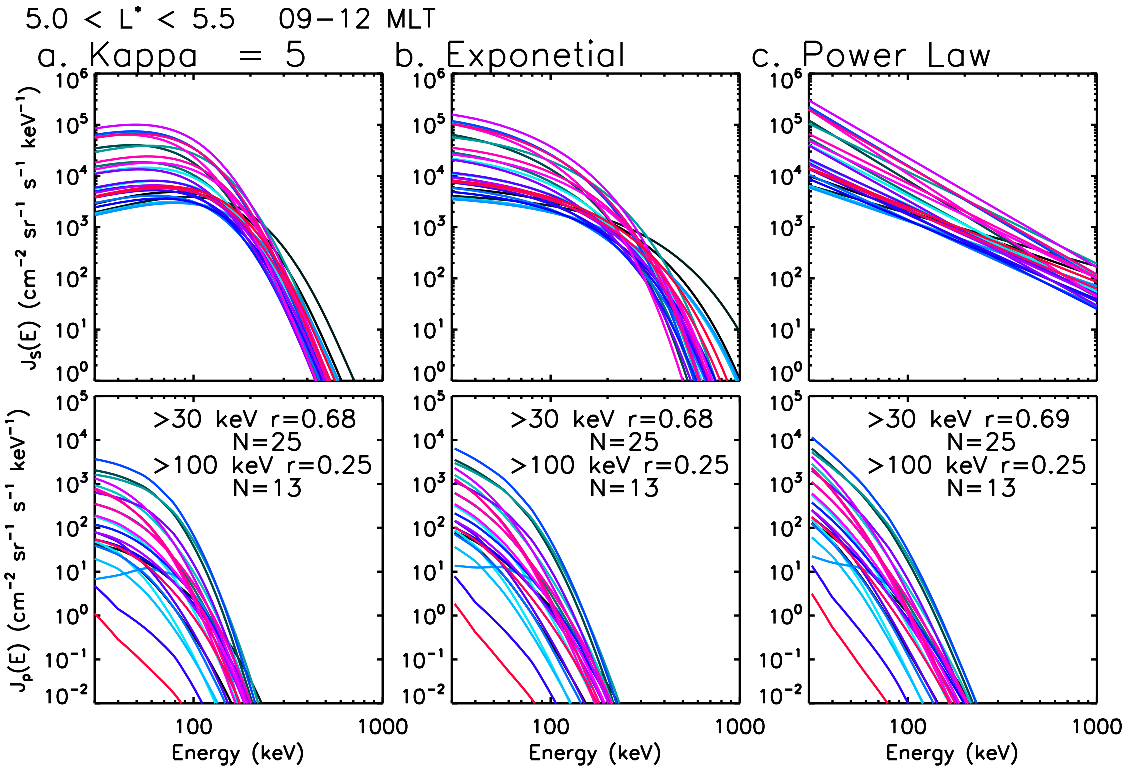

Figure 5. Figure showing the source spectrum (top row) and corresponding calculated precipitating flux spectrum for three different source spectral shapes that have been fitted to the POES T90 data; (a) κ distribution with $\kappa = 5$, (b) Exponential fit, (c) Power law fit between 09-12 MLT, $5 < L^* < 5.5$. The Pearson's linear correlation coefficient and number of points are indicated for each spectra fit for both the >30 and >100 keV channels.

for chorus driven diffusion (e.g. Meredith et al. (2003)). Figure 4 shows for the lower energies (30 keV, 100 keV) we are getting a visible difference in the flux within the field of view of T0 whereas at the highest energy considered (500 keV) the precipitating flux, despite having an almost factor of 10 difference in the source flux (visible in the T90 field of view), is falling off so rapidly in the loss cone, it is outside the pitch angle range measured by the T0 detector at this location. At 250 keV there is very little difference in the differential flux for the different source terms, we can see from Figure 3 there is a cross over in the different spectra around this energy. Figure 4 demonstrates that despite the increase in the source flux at the higher energies, the calculated precipitating flux is highly dependent on the strength of the diffusion coefficients and therefore, according to the Kennel and Petschek (1966) solution, simply increasing the source flux at higher energies will not drastically change the precipitating flux predicted to be measured by the POES T0 detector.

We did a wider test of the different source spectra, using the 26-30 March 2013 event shown in Figure 5; We applied this to all data between $5 < L^* < 5.5$ and 09-12 MLT that are above our noise threshold, (this L^*/MLT region was selected for ease of comparison with data shown in Sections 3.2 and 3.3). We have used three different shapes for the source spectrum fitted to the POES T90 observations: (a) a kappa fit with $\kappa = 5$ (b) an exponential fit and (c) a power law fit and shown the corresponding calculated precipitating spectrum for each time during the event underneath.

Figures 5 clearly shows that the different source terms, whilst having a significant effect on the amount of flux at higher energies, particularly the power law fit, have minimal impact on the calculated T0 precipitating spectra shown for the three source spectral shapes. To further demonstrate this we have included the Pearson's linear correlation coefficient between the calculated and measured T0 precipitating flux on the precipitating spectra graph; these are essentially the same for each source spectra, with the power law giving 0.69 for >30 keV, an improvement of 0.01 compared to the other source terms. As discussed above and shown in Figure 4, this is likely due to the strength of the diffusion coefficients at the higher energies.

3.2 Variability of the cold plasma density

As demonstrated by Figure 4, the strength of the diffusion coefficients have a big impact on the shape of the flux in the loss cone when using the Kennel and Petschek (1966) solution. Therefore, another reason for the underestimate of the >100 keV precipitation in Reidy et al. (2021) could be that the BAS diffusion coefficients are not capturing enough diffusion at higher energies. These diffusion coefficients were calculated as described in Horne et al. (2013) using wave and cold plasma data from seven satellites (Meredith et al., 2020). In this wave data base, the wave parameters are binned by pitch angle, energy, L*, MLT, magnetic latitude, frequency and geomagnetic activity. One of the parameters that go into the diffusion coefficient calculations, provided from this data base, is the cold plasma density, typically discussed as f_{pe}/f_{ce}. The density is known to influence the energy at which resonant wave-particle interactions occur.

To investigate how well the BAS wave model is capturing f_{pe}/f_{ce}, we compare insitu data from RBSP A during November 2012 (an interval where the orbit of RBSP was at high L* on the dawnside; note that this is not possible for the 26-30 March 2013 event as the RBSP were not in the right place), with the f_{pe}/f_{ce} from the BAS wave model that would have been used to calculate the chorus diffusion coefficients (selected at each time based on the RBSP location in L* and MLT and the activity level), shown in the top two panels of Figure 6 respectively. The local f_{pe} measured by the RBSP (top panel of Figure 6) has been projected to the equator assuming a dipole. As in Meredith et al. (2004), the presence of electron cyclotron harmonics (ECH) in the High Frequency Receiver are used to determine if the satellite is outside the plasmapause, indicated at the bottom of the first panel in blue (outside) or red (inside). We only show the f_{pe}/f_{ce} from the BAS wave model when the criteria indicates we are outside the plasmapause as we are interested in chorus waves for this study. It can be seen in general, any time larger values of f_{pe}/f_{ce} are measured, the ECH criteria suggests that the RBSP are inside the plasmapause, though there are a few large values of measured f_{pe}/f_{ce} near the beginning of the month outside the plasmapause during quieter Kp (bottom panel). The modelled f_{pe}/f_{ce} and the ratio of measured to modelled f_{pe}/f_{ce} (third panel) are given when the ECH criteria suggests we are outside the plasmasphere. The modelled f_{pe}/f_{ce} is generally lower than that measured by RBSP during November 2012 with the ratio between the modelled and measured f_{pe}/f_{ce} varying 0.1 - 2.8, with a mean value of 0.8 (red line on panel 3).

To quantify the effect the cold plasma density has on chorus diffusion at the loss cone, we have re-calculated the chorus $D_{\alpha\alpha}(\alpha_0)$ on the dawnside side between $5 < L^* < 5.5$ with f_{pe}/f_{ce} divided by and multiplied by 2, shown in Figure 7 for low, moderate and high Kp. For comparison, chorus $D_{\alpha\alpha}$ calculated with the original f_{pe}/f_{ce} from the BAS wave model is shown in the top panel. It is clear from Figure 7 that dividing f_{pe}/f_{ce} by two increases $D_{\alpha\alpha}$ at the loss cone at the higher energies and multiplying f_{pe}/f_{ce} by two, decreases the diffusion at the higher energies.

The top row of Figure 8 shows calculated precipitating spectra for the 26-30 March 2013 event discussed in Section 3.1 and analysed in Reidy et al. (2021) for $5 < L^* < 5.5$

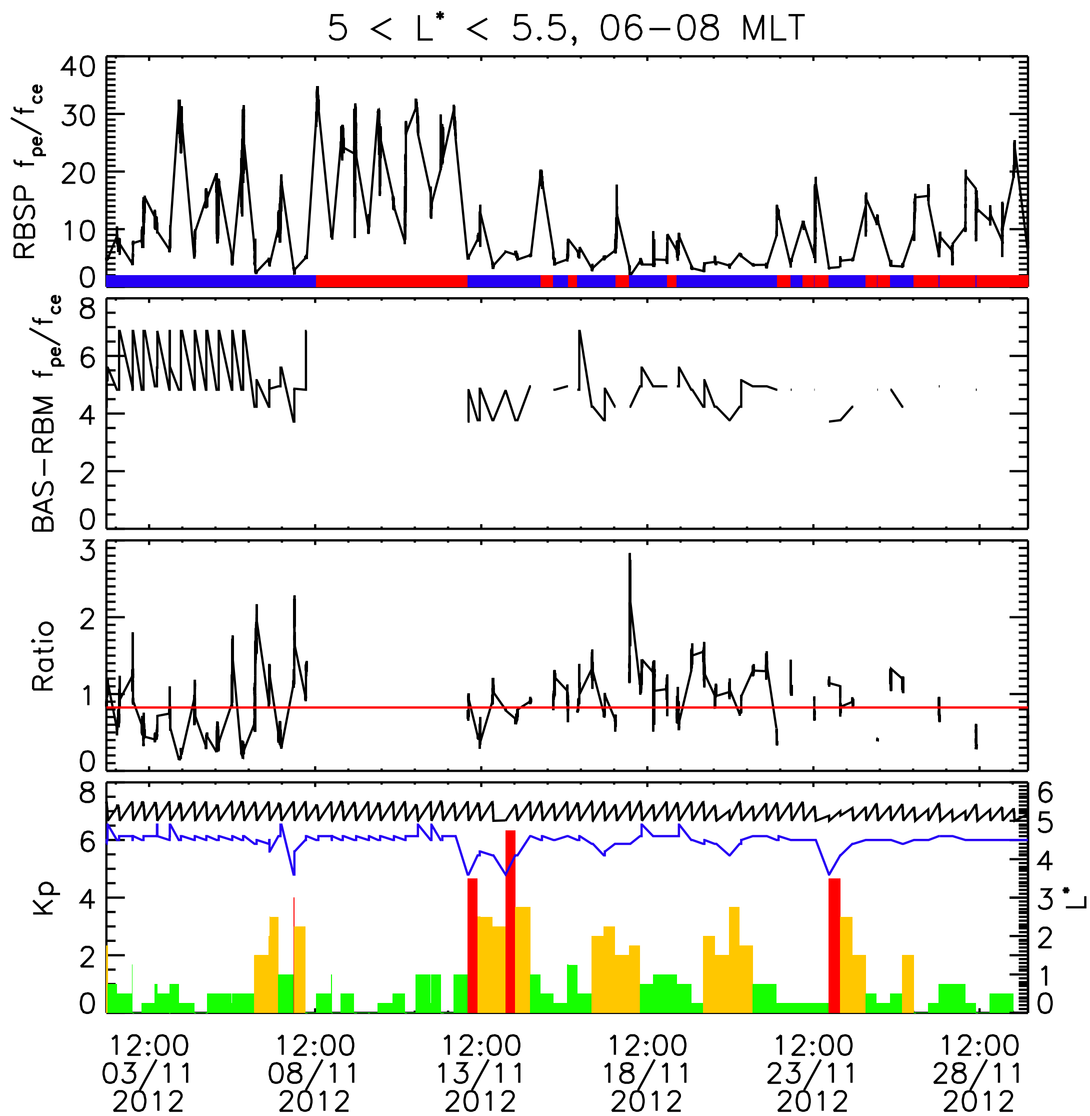

Figure 6. Figure showing the f_{pe}/f_{ce} measured by RBSP-A for 5< L* <5.5, between 06-08 MLT (top panel), the blue and red shading at the bottom of the graph indicate when the ECG criteria suggest the RBSP-A is outside and inside the plasmapause respectively. The f_{pe}/f_{ce} that would be used in the BAS wave model, found using the Kp value and location of the satellite is shown in the second panel, the ratio of the modelled to measured f_{pe}/f_{ce} in the third panel with the mean indicated by the red line. The bottom panel gives the Kp during November 2012 with the colour indicating activity level (green =low activity (0 < Kp< 2), orange = moderate activity (2< Kp <4), and red = high activity, (Kp >4)). The modelled location of the plasmapause (LPP) and the location of the RBSP-A between 06-08 MLT are also shown in the bottom panel by blue and black respectively.

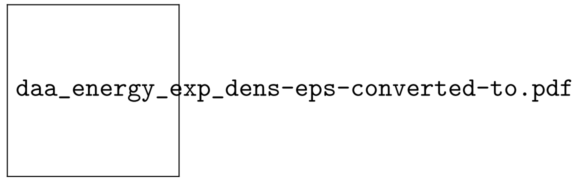

Figure 7. Figure showing MLT verses energy dependence of chorus $D_{\alpha\alpha}$ calculated with the 'original' f_{pe}/f_{ce} from the BAS wave model (top), with f_{pe}/f_{ce} divided by two (middle) and multiplied by 2 (bottom) for low, moderate and high Kp between 06-12 MLT for $5 < L^* < 5.5$.

between 09-12 MLT, for a. chorus $D_{\alpha\alpha}$ with f_{pe}/f_{ce} multiplied by two, b. the original chorus $D_{\alpha\alpha}$ (same as Figure 5a), and c. chorus $D_{\alpha\alpha}$ with f_{pe}/f_{ce} divided by two. These calculations assume a kappa distribution as the source term, with $\kappa = 5$ for a consistent comparison with the earlier Reidy et al. (2021) results. This figure clearly demonstrates that by decreasing the cold plasma density (Figure 8c), the precipitating flux increases at the higher energies and by increasing density (Figure 8a), the flux decreases at the higher energies. The bottom row of Figure 8 shows scatter plots of the measured verses calculated T0 precipitation, with the corresponding Pearson's correlation coefficients for the >30 keV and >100 keV electron channels. These show an improvement for the >100 keV channel when the density is decreased, increasing from 0.25 for the original chorus matrix to 0.37. There is also improvement in the >30 keV with the decreased density. The precipitation calculated using the chorus $D_{\alpha\alpha}$ with f_{pe}/f_{ce} multiplied by two has lower correlation for both electron energy channels. Lines of best fit are also indicated for the >30 keV and >100 keV channels by black and blue dashed lines respectively.

3.3 RBSP-determined diffusion coefficients

Our current method to calculate the precipitation flux relies on diffusion coefficients that were generated using averaged wave models and plasma density. In these models measurements from multiple satellites, such as wave power and cold plasma density, have been binned by location and activity level and then averaged before calculating the diffusion coefficients. However, Watt et al. (2019) showed that if you calculate the diffusion coefficients from co-located measurements and then take an average, there is a significant difference in the diffusion coefficients.

Here we present chorus diffusion coefficients that have been calculated from RBSP data using two different methods, first using average values, as has previously been done (e.g. Horne et al. (2013)) and used above, and secondly by using co-located measurements of the wave spectra and f_{pe}/f_{ce} to calculate $D_{\alpha\alpha}$ and then averaging, similar to that presented in Ross et al. (2021) for EMIC waves and Wong et al. (2022) for magnetosonic waves. Both methods use a modified version of the PADIE code (Glauert & Horne, 2005) which allows an arbitrary wave power spectral density input rather than Gaussian inputs. We have concentrated on the dawnside between 00-12 MLT, for $5 < L^* < 5.5$ as this is where we have RBSP measurements and chorus scattering is known to occur (e.g. Lam et al. (2010)). We have used the same field line model (Olson & Pfitzer, 1977) used in Reidy et al. (2021) for continuity and the ECH criteria from Meredith et al. (2004) is employed to determine if the satellites are outside the plasmapause. The RBSP chorus diffusion coefficient matrices are computed by combining RBSP data with a profile for how chorus wave power changes with latitude, derived from the VLF database in Meredith et al. (2018). The magnetic latitude profile enables us to map RBSP measurements to magnetic latitudes between $0 < \text{MLAT} < 60$ and therefore include the effects of high latitude chorus in our results. The RBSP diffusion matrices also use a new chorus wave nor-

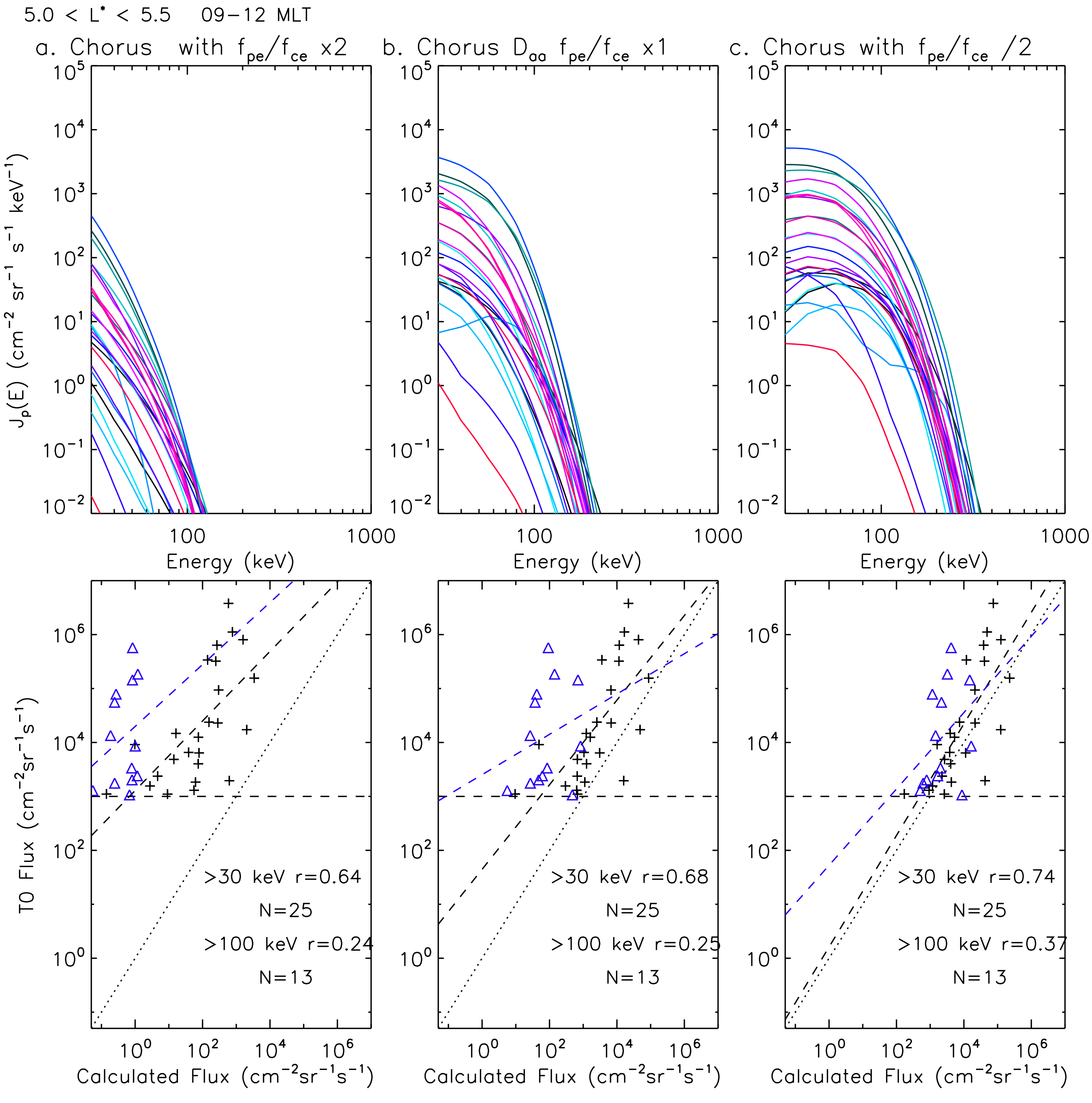

Figure 8. Calculated precipitating spectra and corresponding scatter plot of measured verses T0 flux for chorus $D_{\alpha\alpha}$ calculated with: (a) f_{pe}/f_{ce} multiplied by 2, (b) the f_{pe}/f_{ce} currently used to calculate the diffusion coefficients (c) f_{pe}/f_{ce} divided by two for the 26-30 March 2013 event between 09-12 MLT for $5 < L^* < 5.5$. The number of points analysed for each POES energy channel (>30 keV and >100 keV) and the Pearson's linear correlation coefficient is given for each case on the scatter plot as well as the line of best fit for the >30 keV (black) and >100 keV (blue) channels indicated by dashed lines. The x=y line is indicated by a dotted line to help comparison.

mal angle model derived from RBSP data composed of different wave normal angle distributions for different spatial location and f_{pe}/f_{ce} bins.

Figure 9 shows chorus-driven $D_{\alpha\alpha}$ at the edge of the loss cone as a function of MLT and energy between 5 < L* <5.5 for different activity levels. The top row were calculated using the wave data base described in Meredith et al. (2020) (used in Reidy et al. (2021)), included here for comparison and are the same as Figure 7a for a wider MLT range. The middle row is using the same method of calculation for the $D_{\alpha\alpha}$ but only using RBSP data. The bottom row show $D_{\alpha\alpha}$ calculated using co-located measurements from the RBSPs. The biggest differences in the chorus $D_{\alpha\alpha}(\alpha_0)$, are seen in the change from using the entire wave data base to the RBSP data, with some smaller differences due to changes in the method of calculating the RBSP chorus, especially for low Kp.

Figure 10 shows a cut through at 100 keV for the three different methods of calculating chorus-driven $D_{\alpha\alpha}$ at the loss cone for low, moderate and high Kp. For moderate activity (i.e. 2< Kp <3), all the three methods produce similar $D_{\alpha\alpha}$, with the RBSP chorus using co-located measurements being slightly higher in general. The biggest difference can be seen for the low Kp, however due to the flux noise threshold we use for the POES measurements, we do not calculate the precipitation during low Kp (see Figure 1) and for high Kp MLT < 4 where the RBSP $D_{\alpha\alpha}(\alpha_0)$ for both methods is significantly higher than the $D_{\alpha\alpha}(\alpha_0)$ using the entire wave data base at 100 keV.

Figure 11 shows the calculated precipitating spectra (top) and the measured verses the calculated precipitation fluxes (bottom) between 09-12 MLT, 5 < L* < 5.5 between 24-30 March 2013, and is comparable to Figures 5 and 8. As in Section 3.2, we are using the $\kappa = 5$ model for the source spectrum for continuity of comparison. Figures 11a, b and c show the results using the diffusion coefficients calculated using the entire wave data base and then the averaged and co-located RBSP measurements respectively. The precipitating spectra is harder for the RBSP-observation determined chorus $D_{\alpha\alpha}$, which has in turn increased the calculated T0 flux for the >100 keV channel, improving the linear correlation from 0.25 to 0.46 and 0.44 for the averaged and co-located methods respectively. These are much larger increases in the correlation coefficient for the 100 keV channel compared to changing the source spectrum (which made very little difference) and by artificially decreasing the density by 2 (which increased the 100 keV correlation to 0.37).

Figure 12 shows the Pearson's linear correlation coefficient between the measured and calculated T0 flux for the three different methods of calculating the chorus diffusion coefficients for >30 keV electrons (a-c) and >100 keV electrons (d-f) for $5 < L^* < 5.5$ between 0-12 MLT. The correlation is only shown for a confidence level above 80% for the >100 keV channel and above 95% for the >30 keV. For reference, the Pearson's correlation coefficient for both T0 electron energy channels and each MLT sector are given in Table 2. For all the MLT sectors, except 00-03 MLT for the >100 keV channel, the use of the RBSP-observation determined chorus $D_{\alpha\alpha}$ has increased the correlation for both the >30 keV and >100 keV channels compared to using the all chorus wave data base. For the >30 keV channel, the RBSP co-located chorus $D_{\alpha\alpha}$ produce the best comparison results between the calculation and observation, however the >100 keV comparison is only better for MLT<6, where the RBSP averaged $D_{\alpha\alpha}$ are best.

4 Discussion

In this paper we have explored the 'missing' higher energy precipitation in the calculations presented by Reidy et al. (2021). We have investigated the impact of the spectral shape used as the source term with conjugate measurements from GOES-15 as well as the effect of the variability of the cold plasma density and the method of calculation on the strength of the chorus diffusion coefficients at the edge of the loss cone.

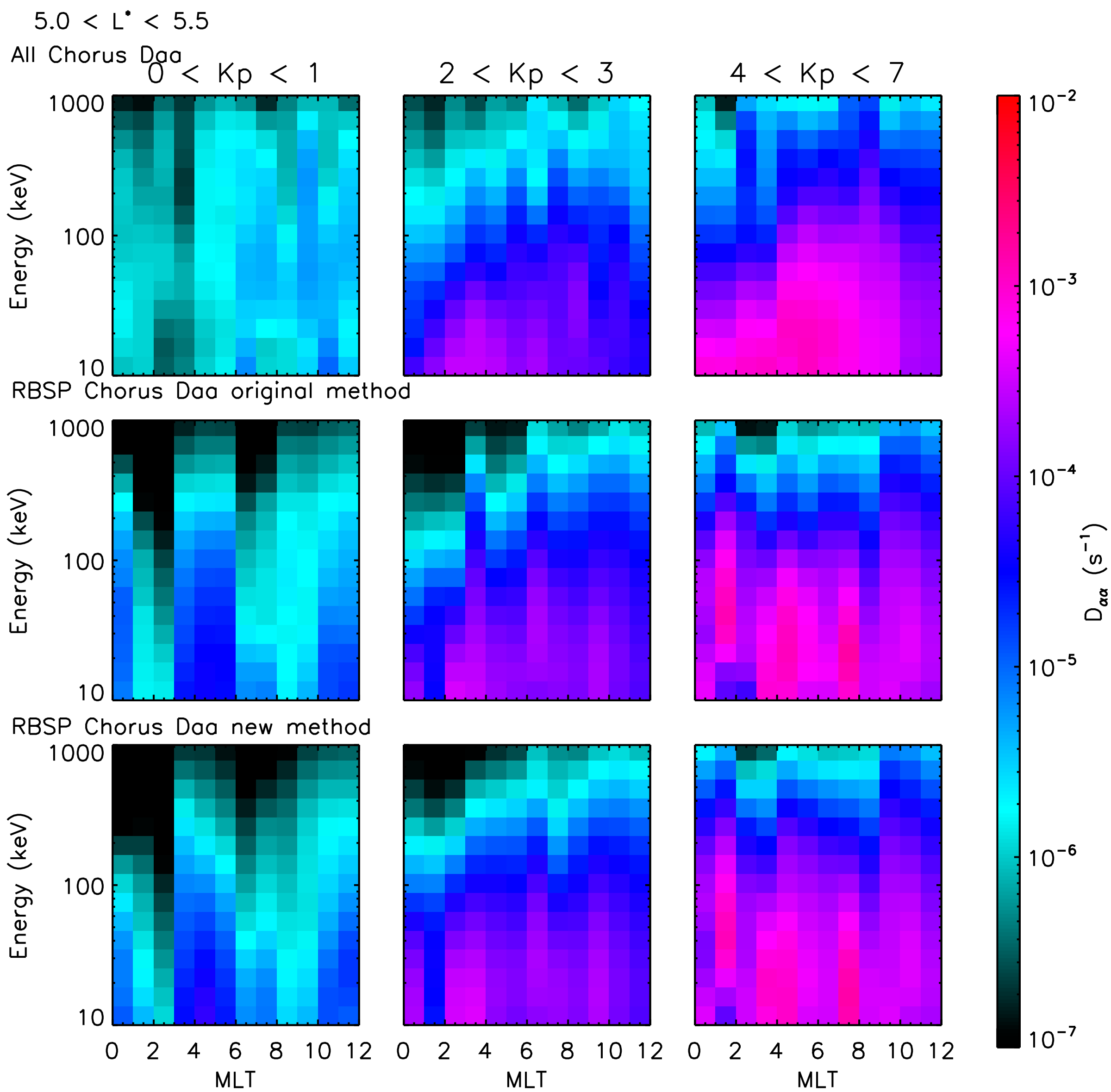

Figure 9. MLT- energy distribution for chorus pitch angle diffusion coefficients evaluated at the loss cone which have been calculated using average values from all the chorus wave data presented in Meredith et al. (2020) (top row), using average values measured by RBSP (middle row) and using co-located measurements of the wave spectra and f_{pe}/f_{ce} from RBSP (bottom) during low, moderate and high Kp levels.

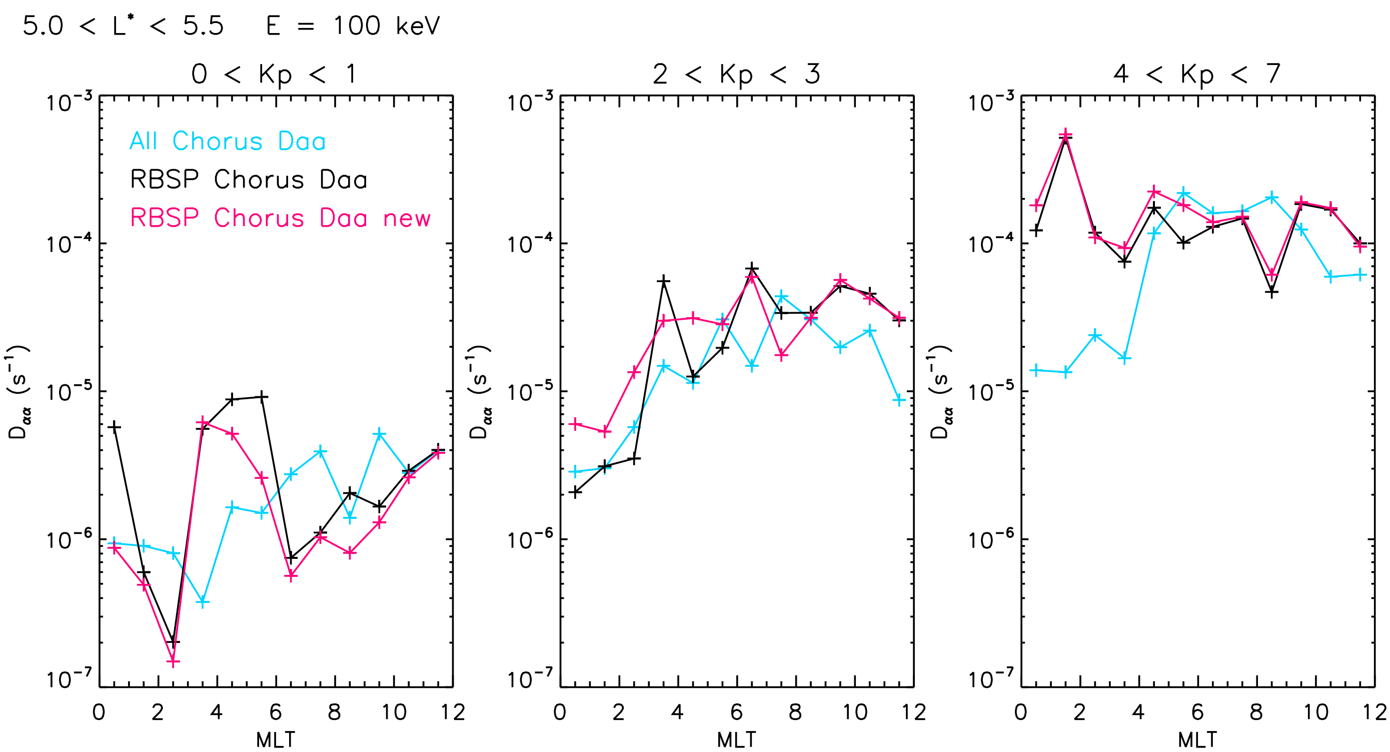

Figure 10. Chorus-driven pitch angle diffusion coefficients for electrons at 100 keV for different MLT sectors and low, moderate and high Kp levels. Shown for three different calculations: All chorus $D_{\alpha\alpha}$ (blue), RBSP $D_{\alpha\alpha}$ average calculation (black), RBSP $D_{\alpha\alpha}$ co-located measurements (pink).

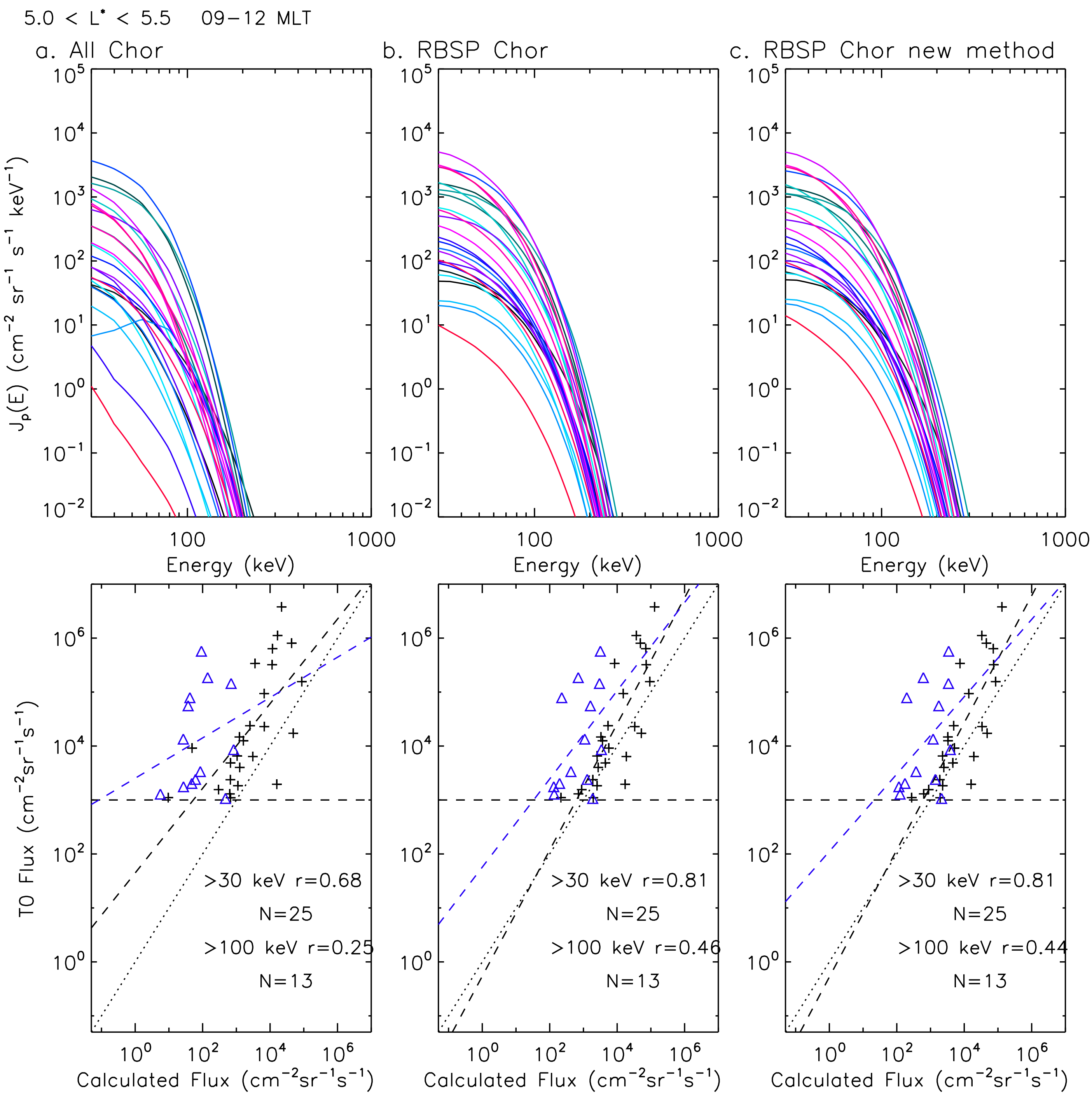

Figure 11. The precipitating spectra (top) and corresponding measured verses calculated T0 flux (bottom) between 09-12 MLT, $5 < L^* < 5.5$ between 26-30 March 2013 for chorus diffusion calculated using (a) All the wave data from Meredith et al. (2020), (b) The RBSP data and (c) The RBSP data using co-located rather than average measurements of the wave power and f_{ce}/f_{pe}. The Pearson's correlation coefficients and number of points is shown on the scatter plot for each case, as well as a line of best fit for the >30 keV and >100 keV channels in black and blue dashed lines respectively with the x=y indicated by a dotted line for comparison.

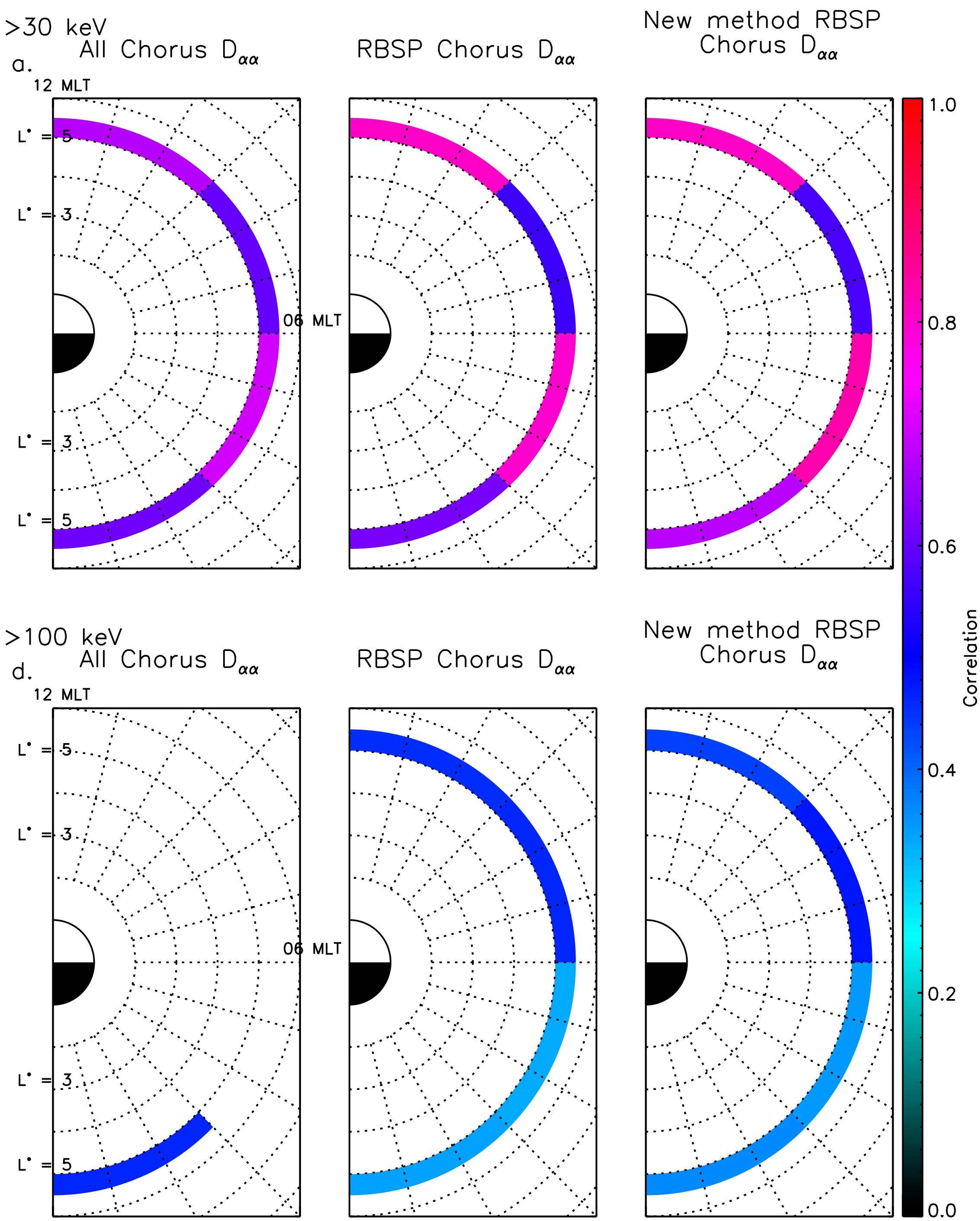

Figure 12. Dial plots between 00-12 MLT with noon at the top and dawn to the right, showing the Pearson's correlation coefficient between the measured and calculated T0 flux for different MLT sectors between $5 < L^* < 5.5$ for the >30 keV channel (top row) and the >100 keV channel (bottom row) using chorus diffusion coefficients calculated in three ways. The correlation is shown for at 95% and 80% confidence levels for the >30 and >100 keV channels respectively.

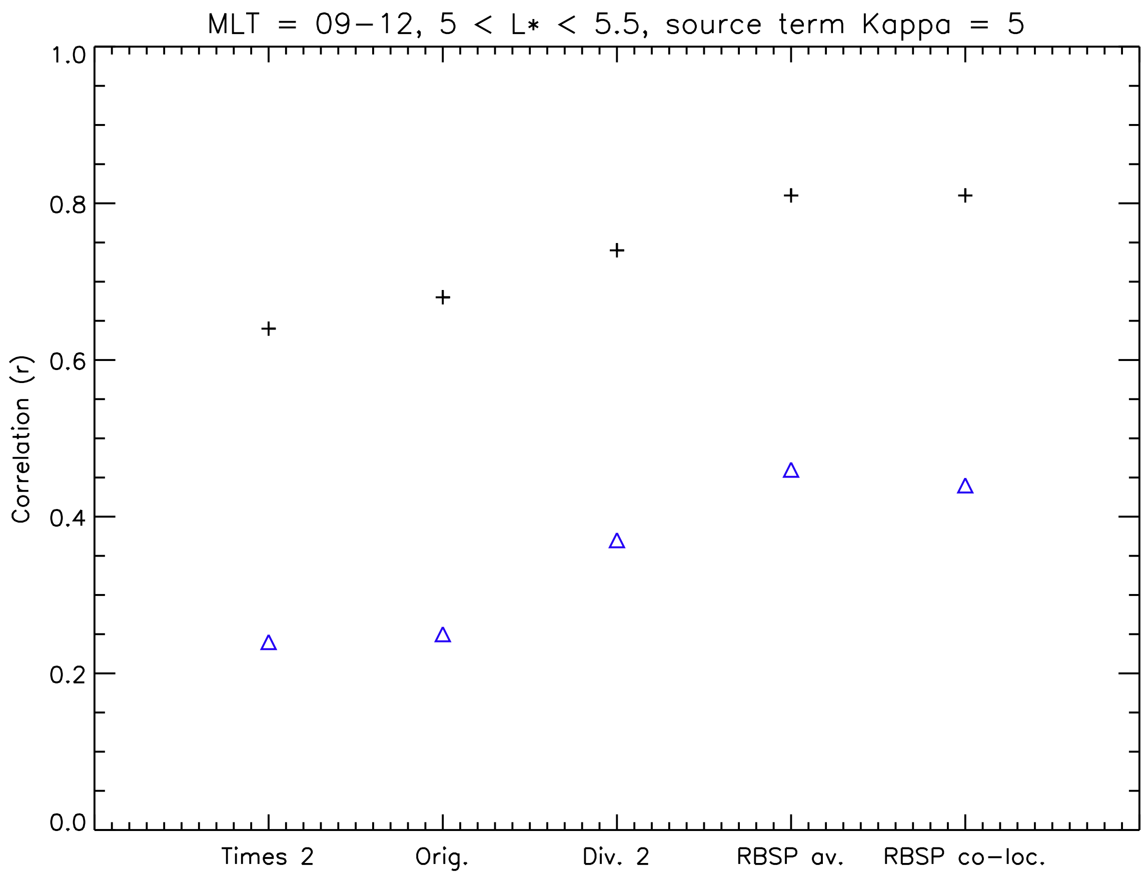

Figure 13. The Pearson's linear correlation coefficients for the calculated and measured >30 and >100 keV T0 in black crosses and blue triangles respectively where the T0 flux has been calculated using the Chorus diffusion matrix with f_{pe}/f_{ce} times by 2 ("Times 2"), the original matrix used in Reidy et al. (2021) ("Orig."), with f_{pe}/f_{ce} divided by 2 ("Div 2"), using averaged wave measurements solely from RBSP (as opposed to the entire wave data base) ("RBSP av") and lastly using co-located RBSP wave measurements ("RBSP co-loc").

$5 < L^* < 5.5$	All chorus $D_{\alpha\alpha}$ >30 keV	>100 keV	Av. RBSP chorus $D_{\alpha\alpha}$ >30 keV	>100 keV	co-located RBSP chorus $D_{\alpha\alpha}$ >30 keV	>100 keV
00-03 MLT	0.61	0.46	0.62	0.34	0.68	0.37
03-06 MLT	0.71	0.11	0.80	0.33	0.83	0.37
06-09 MLT	0.60	0.07	0.56	0.46	0.57	0.35
09-12 MLT	0.68	0.25	0.81	0.46	0.81	0.44

Table 2. Pearson's linear correlation coefficient for the measured to calculated T0 precipitating flux between 24-30 March for $5 < L^* < 5.5$ in three hours of MLT bins on the dawnside for >30 keV and >100 keV electron integral flux channels using the three different methods of calculating chorus $D_{\alpha\alpha}$.

Figure 13 shows the Pearson's linear correlation coefficients between the measured and calculated T0 flux using five different variations of chorus-driven diffusion coefficient, all with a $\kappa = 5$ source term. We see a clear improvement in our results, for both >30 keV (black crosses) and >100 keV (blue triangles) energy channels when we decrease the plasma density used in the calculation of the chorus-driven diffusion caused precipitation. This suggests the density used within the BAS model may be too high; similarly, Longley et al. (2022) used the ratio between the precipitating and trapped flux observed by POES on 17 March 2013 to infer a generally lower plasma density than used in BAS-RBM. The next improvement in correlation values seen in Figure 13 comes from using solely RBSP data (as opposed to the averaging approach employing the entire BAS wave data base) to calculate the diffusion coefficients, almost doubling the correlation coefficient for the higher energy channel from 0.25 to 0.46. We suggest these results may also be explained by the potential overestimate in the plasma density in the entire wave data base due to the inclusion of THEMIS data. THEMIS infers the total electron density using measurements of the spacecraft potential (from the electric field instrument) and the electron thermal speed (from the electrostatic analyser) (Mozer, 1973; Pedersen et al., 1998). The resulting electron densities are associated with a factor of $\tilde{2}$ uncertainty (Li et al., 2010). In contrast it has been found that the EMFISIS/RBSP electron density measurements are more accurate than those determined using spacecraft potential to estimate the density, as this approach reduces uncertainties due to the effects of cold electron temperatures (Wygant et al., 2013). Therefore, the density measurements from THEMIS included in the entire wave database could result in an inaccurate/higher plasma density than we are seeing from solely using the RBSP data leading to the better correlation in our results we see from using the RBSP derived diffusion coefficients. Figure 13 also shows we are getting slightly better results using the average method of calculation opposed to using co-located measurements. This is in contrast to Ross et al. (2020, 2021), who found using EMIC $D_{\alpha\alpha}$ calculated with co-located rather than averaged measurements, provided better agreement with modelled data from the BAS-RBM and similarly Wong et al. (2022) found co-located measurements of magnetosonic waves improved their results. However, these studies were looking at different pitch angles where perhaps the difference in variability within bins makes a larger difference to the diffusion coefficient calculation.

For completeness, Table 3 details the Pearson's linear correlation coefficient for the calculated and measured precipitation in the >30 and >100 keV POES flux channels, between 09-12 MLT and 5 $5 < L^* < 5.5$, for each of the tests we present in this paper, and previously shown in Figures 5, 8, 11. In this table we have also included results calculated using the different source terms with the two RBSP-observation determined chorus diffusion coefficients which are not shown. As discussed above, we get the biggest improvement to the results found in Reidy et al. (2021) (top row of Table 3), when we are using chorus $D_{\alpha\alpha}(\alpha_0)$ calculated using averaged RBSP data with either a Power law

Chorus $D_{\alpha\alpha}$ matrix	Source term	r_{30}	r_{100}
All Chorus	$\kappa = 5$	0.68	0.25
All Chorus	$\kappa = 2$	0.68	0.25
All Chorus	Exponential	0.68	0.25
All Chorus	Power Law	0.69	0.26
f_{pe}/f_{ce} x2	$\kappa = 5$	0.64	0.24
f_{pe}/f_{ce} ÷2	$\kappa = 5$	0.74	0.37
Av. RBSP	$\kappa = 5$	0.81	0.46
Av. RBSP	$\kappa = 2$	0.81	0.46
Av. RBSP	Exponential	0.81	0.45
Av. RBSP	Power Law	0.82	0.45
Co. loc. RBSP	$\kappa = 5$	0.81	0.44
Co. loc. RBSP	$\kappa = 2$	0.81	0.43
Co. loc. RBSP	Exponential	0.81	0.43
Co. loc. RBSP	Power Law	0.81	0.43

Table 3. Pearson's linear correlation coefficient between the measured and calculated T0 precipitating fluxes between 24-30 March 2013 for $5 < L^* < 5.5$ between 09-12 MLT. in three hours of MLT bins on the dawnside for >30 keV (r_{30}) and >100 keV (r_{100}) electron integral flux channels using the different source terms and chorus diffusion methods in our calculation. All Chorus refers to the chorus matrix calculated using the entire wave data base, av. RBSP and co. loc. RBSP differentiates between the chorus diffusion matrices calculated using averaged and co-located RBSP measurements.

or Kappa source spectrum; we have increased our correlation between the measured and calculated T0 precipitation in this region from 0.68 to 0.82 for the >30 keV channel and from 0.25 to 0.46 in the >100 keV channel. It is not a straight forward answer which source spectrum is best, with a power law giving the best results for the >30 keV channel and a kappa fit being best for the >100 keV channel. However, we have shown the changes in source spectral shape are minimal compared with which chorus diffusion matrix is applied when using the Kennel and Petschek (1966) solution to calculate the T0 precipitation (as presented in this paper); it is known the spectral shape is of great importance when considering the precipitation using other methods/ instruments, as shown for example in Clilverd et al. (2010, 2017).

The improved correlation in our results for the >100 keV channel is still considerably less than the correlation found for the >30 keV channel (0.46 compared to 0.82), therefore we are still likely missing something at the higher energies. In Kurth et al. (2015b) they give details on how the electron density are determined from the plasma wave spectrum measured by EMFSIS. They note limitations in identifying the upper hybrid band during geomagnetically active times, when the electron densities are low; during these times they 'fail to identify any spectral features' and leave a gap in the data set. Therefore this could lead to a systematic bias in the RBSP plasma density whereby periods of low plasma density, when the diffusion will be higher, are being excluded. This is because the density shifts the resonance energy, whereby lower densities result in more diffusion at the higher energies, as discussed by Allison et al. (2021) and demonstrated in Figure 7 where decreasing the density has increased the diffusion coefficients at the higher energies and increasing the density increases the diffusion coefficients at the lower energies. The inclusion of this lower density data from RBSP could therefore increase the diffusion rates and provide the extra diffusion we are missing at the higher energies, however determining such is an extensive piece of work which we leave to future studies. Other avenues to improve our results include using a more dynamic geomagnetic field model, such as TS04 (Tsyganenko & Sitnov, 2005) (rather than Olson Ptizer Quiet model which is for quiet geomagnetic times), to calculate L* and our diffusion coefficients, particularly considering our results are primarily from periods with moderate to high Kp. Furthermore, as stated in Reidy et al. (2021), we are using averaged rather than event-specific diffusion coefficients to calculate precipitation during an event and therefore analysing over more events may provide us with a bigger picture and improve our results. Lastly, it is possible that highly non-linear effects, which are not included in quasi-linear theory, could enhance the diffusion and increase the precipitation.

5 Conclusion

In this study we have have improved on the calculated T0 precipitating fluxes presented earlier in Reidy et al. (2021), on the dawnside particularly for the higher energies by using $D_{\alpha\alpha}$ calculated from RBSP measurements. We have investigated the method of calculation by experimenting with different source spectral shapes, as well as different versions of the BAS chorus-driven diffusion matrix. The key results of this paper can be summarised as follows:

- Using our current method of calculation (the Kennel and Petschek (1966) solution to the diffusion equation), increasing the hardness of the source spectrum has a minimal effect on the amount of calculated T0 precipitation.
- We have demonstrated that using chorus diffusion coefficients that have been calculated assuming a lower cold plasma density (f_{pe}/f_{ce} divided by 2) significantly increases the precipitation at higher energies, towards the magnitudes which are closer to those observed. This is because reducing the cold plasma density increases the diffusion rates at higher energies and results in more particles being precipitated.
- We have found that using chorus $D_{\alpha\alpha}(\alpha_0)$ calculated with RBSP data improves our results compared to chorus $D_{\alpha\alpha}(\alpha_0)$ calculated from data compiled from many satellites (presented in Meredith et al. (2020)). This is most likely due to the more accurate wave measurements from RBSP than other spacecraft included in the whole BAS model (e.g. THEMIS).
- We still find there is a better correlation between the calculations with the POES T0 >30 keV electron channel measurements compared to that for the >100 keV channel, suggesting there is still some missing diffusion at the higher energies.

6 Open Research

The POES particle data used in this study came from NOAA National Geophysical Data Centre for the (`https://ngdc.noaa.gov/stp/satellite/poes/dataaccess.html`). The Kp indices were downloaded from the OMNI database (`https://omniweb.gsfc.nasa.gov/`). The Chorus wave pitch angle diffusion coefficients calculated for use in this study have been published in the Polar Data Centre (`https://doi.org/10.5285/5ef0d6cd-67c2-48fc-8a6a-dfe44a63979e`) (Reidy et al., 2023).

References

Allison, H. J., Shprits, Y. Y., Zhelavskaya, I. S., Wang, D., & Smirnov, A. G. (2021, January). Gyroresonant wave-particle interactions with chorus waves during extreme depletions of plasma density in the Van Allen radiation belts. *Science Advances*, *7*(5), eabc0380. doi: 10.1126/sciadv.abc0380

Clilverd, M. A., Rodger, C. J., Gamble, R. J., Ulich, T., Raita, T., SeppäLä, A., ... Parrot, M. (2010, December). Ground-based estimates of outer radiation belt energetic electron precipitation fluxes into the atmosphere. *Journal of Geophysical Research (Space Physics)*, *115*(A12), A12304. doi:

10.1029/2010JA015638

Clilverd, M. A., Rodger, C. J., McCarthy, M., Millan, R., Blum, L. W., Cobbett, N., ... Halford, A. J. (2017, January). Investigating energetic electron precipitation through combining ground-based and balloon observations. *Journal of Geophysical Research (Space Physics)*, *122*(1), 534-546. doi: 10.1002/2016JA022812

Evans, D., & Greer, M. (2004, 01). Polar orbiting environmental satellite space environment monitor - 2 instrument descriptions and archive data documentation. *NOAA Tech. Memo. 1.4*.

Ferradas, C. P., Jordanova, V. K., Reeves, G. D., & Larsen, B. A. (2019). Comparison of electron loss models in the inner magnetosphere during the 2013 st. patrick's day geomagnetic storm. *Journal of Geophysical Research: Space Physics*, *124*(10), 7872-7888. Retrieved from `https://agupubs.onlinelibrary.wiley.com/doi/abs/10.1029/2019JA026649` doi: 10.1029/2019JA026649

Glauert, S. A., & Horne, R. B. (2005, Apr). Calculation of pitch angle and energy diffusion coefficients with the PADIE code. *Journal of Geophysical Research (Space Physics)*, *110*(A4), A04206. doi: 10.1029/2004JA010851

Glauert, S. A., Horne, R. B., & Meredith, N. P. (2014, Jan). Three-dimensional electron radiation belt simulations using the BAS Radiation Belt Model with new diffusion models for chorus, plasmaspheric hiss, and lightning-generated whistlers. *Journal of Geophysical Research (Space Physics)*, *119*(1), 268-289. doi: 10.1002/2013JA019281

Glauert, S. A., Horne, R. B., & Meredith, N. P. (2018). A 30-year simulation of the outer electron radiation belt. *Space Weather*, *16*(10), 1498-1522. Retrieved from `https://agupubs.onlinelibrary.wiley.com/doi/abs/10.1029/2018SW001981` doi: 10.1029/2018SW001981

Horne, R. B., Kersten, T., Glauert, S. A., Meredith, N. P., Boscher, D., Sicard-Piet, A., ... Li, W. (2013, October). A new diffusion matrix for whistler mode chorus waves. *Journal of Geophysical Research (Space Physics)*, *118*(10), 6302-6318. doi: 10.1002/jgra.50594

Jordanova, V. K., Tu, W., Chen, Y., Morley, S. K., Panaitescu, A. D., Reeves, G. D., & Kletzing, C. A. (2016, September). RAM-SCB simulations of electron transport and plasma wave scattering during the October 2012 "double-dip" storm. *Journal of Geophysical Research (Space Physics)*, *121*(9), 8712-8727. doi: 10.1002/2016JA022470

Kennel, C. F., & Petschek, H. E. (1966). Limit on Stably Trapped Particle Fluxes. *Journal of Geophysical Research*, *71*, 1. doi: 10.1029/JZ071i001p00001

Kletzing, C. A., Kurth, W. S., Acuna, M., MacDowall, R. J., Torbert, R. B., Averkamp, T., ... Tyler, J. (2013). The Electric and Magnetic Field Instrument Suite and Integrated Science (EMFISIS) on RBSP. *Space Science Review*, *179*(1-4), 127-181. doi: 10.1007/s11214-013-9993-6

Kurth, W. S., De Pascuale, S., Faden, J. B., Kletzing, C. A., Hospodarsky, G. B., Thaller, S., & Wygant, J. R. (2015a, February). Electron densities inferred from plasma wave spectra obtained by the Waves instrument on Van Allen Probes. *Journal of Geophysical Research (Space Physics)*, *120*(2), 904-914. doi: 10.1002/2014JA020857

Kurth, W. S., De Pascuale, S., Faden, J. B., Kletzing, C. A., Hospodarsky, G. B., Thaller, S., & Wygant, J. R. (2015b, February). Electron densities inferred from plasma wave spectra obtained by the Waves instrument on Van Allen Probes. *Journal of Geophysical Research (Space Physics)*, *120*(2), 904-914. doi: 10.1002/2014JA020857

Lam, M. M., Horne, R. B., Meredith, N. P., Glauert, S. A., Moffat-Griffin, T., & Green, J. C. (2010). Origin of energetic electron precipitation >30 keV into the atmosphere. *Journal of Geophysical Research (Space Physics)*, *115*(8),

A00F08. doi: 10.1029/2009JA014619
Li, W., Ni, B., Thorne, R. M., Bortnik, J., Green, J. C., Kletzing, C. A., ... Hospodarsky, G. B. (2013). Constructing the global distribution of chorus wave intensity using measurements of electrons by the poes satellites and waves by the van allen probes. *Geophysical Research Letters*, *40*(17), 4526-4532. Retrieved from `https://agupubs.onlinelibrary.wiley.com/doi/abs/10.1002/grl.50920` doi: 10.1002/grl.50920
Li, W., Thorne, R. M., Bortnik, J., Nishimura, Y., Angelopoulos, V., Chen, L., ... Bonnell, J. W. (2010, December). Global distributions of suprathermal electrons observed on THEMIS and potential mechanisms for access into the plasmasphere. *Journal of Geophysical Research (Space Physics)*, *115*(A12), A00J10. doi: 10.1029/2010JA015687
Longley, W. J., Chan, A. A., Jaynes, A. N., Elkington, S. R., Pettit, J. M., Ross, J. P. J., ... Horne, R. B. (2022, November). Using MEPED observations to infer plasma density and chorus intensity in the radiation belts. *Frontiers in Astronomy and Space Sciences*, *9*, 1063329. doi: 10.3389/fspas.2022.1063329
Mauk, B. H., Fox, N. J., Kanekal, S. G., Kessel, R. L., Sibeck, D. G., & Ukhorskiy, A. (2013). Science Objectives and Rationale for the Radiation Belt Storm Probes Mission. *Space Science Review*, *179*(1-4), 3-27. doi: 10.1007/s11214-012-9908-y
Meredith, N. P., Horne, R. B., Kersten, T., Li, W., Bortnik, J., Sicard, A., & Yearby, K. H. (2018, June). Global Model of Plasmaspheric Hiss From Multiple Satellite Observations. *Journal of Geophysical Research (Space Physics)*, *123*(6), 4526-4541. doi: 10.1029/2018JA025226
Meredith, N. P., Horne, R. B., Shen, X.-C., Li, W., & Bortnik, J. (2020). Global Model of Whistler Mode Chorus in the Near-Equatorial Region ($|\lambda_m| < 18°$). *Geophysical Research Letters*. doi: 10.1002/2020GL087311
Meredith, N. P., Horne, R. B., Thorne, R. M., & Anderson, R. R. (2003). Favored regions for chorus-driven electron acceleration to relativistic energies in the Earth's outer radiation belt. *Geophysical Research Letters*, *30*(16). Retrieved from `https://agupubs.onlinelibrary.wiley.com/doi/abs/10.1029/2003GL017698` doi: 10.1029/2003GL017698
Meredith, N. P., Horne, R. B., Thorne, R. M., Summers, D., & Anderson, R. R. (2004, June). Substorm dependence of plasmaspheric hiss. *Journal of Geophysical Research (Space Physics)*, *109*(A6), A06209. doi: 10.1029/2004JA010387
Mozer, F. S. (1973, February). Analysis of Techniques for Measuring DC and AC Electric Fields in the Magnetosphere. *Space Science Review*, *14*(2), 272-313. doi: 10.1007/BF02432099
Nesse Tyssøy, H., Sandanger, M. I., Ødegaard, L.-K. G., Stadsnes, J., Aasnes, A., & Zawedde, A. E. (2016). Energetic electron precipitation into the middle atmosphere constructing the loss cone fluxes from meped poes. *Journal of Geophysical Research: Space Physics*, *121*(6), 5693-5707. Retrieved from `https://agupubs.onlinelibrary.wiley.com/doi/abs/10.1002/2016JA022752` doi: 10.1002/2016JA022752
Olson, W. P., & Pfitzer, K. A. (1977). Magnetospheric magnetic field modeling. annual scientific report. *Air Force Off. of Sci. Res.*.
Onsager, T., Grubb, R., Kunches, J., Matheson, L., Speich, D., Zwickl, R. W., & Sauer, H. (1996, October). Operational uses of the GOES energetic particle detectors. In E. R. Washwell (Ed.), *Goes-8 and beyond* (Vol. 2812, p. 281-290). doi: 10.1117/12.254075
Pedersen, A., Mozer, F., & Gustafsson, G. (1998, January). Electric Field Measurements in a Tenuous Plasma with Spherical Double Probes. *Geophysical Monograph Series*, *103*, 1. doi: 10.1029/GM103p0001
Reidy, J., Ross, J., & Wong, J. (2023). Pitch angle diffusion coefficients used in comparison of quasi-linear diffusion theory with in-situ measurements (Ver-

sion 1.0) [Data set]. *NERC EDS UK Polar Data Centre*. Retrieved from https://doi.org/10.5285/5ef0d6cd-67c2-48fc-8a6a-dfe44a63979e

Reidy, J. A., Horne, R. B., Glauert, S. A., Clilverd, M. A., Meredith, N. P., Woodfield, E. E., ... Rodger, C. J. (2021). Comparing electron precipitation fluxes calculated from pitch angle diffusion coefficients to leo satellite observations. *Journal of Geophysical Research: Space Physics*, *126*(3), e2020JA028410. doi: https://doi.org/10.1029/2020JA028410

Ripoll, J. F., Loridan, V., Denton, M. H., Cunningham, G., Reeves, G., Santolík, O., ... Ukhorskiy, A. Y. (2019). Observations and Fokker-Planck Simulations of the L-Shell, Energy, and Pitch Angle Structure of Earth's Electron Radiation Belts During Quiet Times. *Journal of Geophysical Research (Space Physics)*, *124*(2), 1125-1142. doi: 10.1029/2018JA026111

Rodger, C. J., Carson, B. R., Cummer, S. A., Gamble, R. J., Clilverd, M. A., Green, J. C., ... Berthelier, J.-J. (2010). Contrasting the efficiency of radiation belt losses caused by ducted and nonducted whistler-mode waves from ground-based transmitters. *Journal of Geophysical Research: Space Physics*, *115*(A12). Retrieved from https://agupubs.onlinelibrary.wiley.com/doi/abs/10.1029/2010JA015880 doi: 10.1029/2010JA015880

Rodger, C. J., Clilverd, M. A., Green, J. C., & Lam, M. M. (2010). Use of POES SEM-2 observations to examine radiation belt dynamics and energetic electron precipitation into the atmosphere. *Journal of Geophysical Research: Space Physics*, *115*(A4). Retrieved from https://agupubs.onlinelibrary.wiley.com/doi/abs/10.1029/2008JA014023 doi: 10.1029/2008JA014023

Rodger, C. J., Clilverd, M. A., Hendry, A. T., & Forsyth, C. (2022). Examination of radiation belt dynamics during substorm clusters: Magnetic local time variation and intensity of precipitating fluxes. *Journal of Geophysical Research: Space Physics*, *127*(12), e2022JA030750. Retrieved from https://agupubs.onlinelibrary.wiley.com/doi/abs/10.1029/2022JA030750 (e2022JA030750 2022JA030750) doi: https://doi.org/10.1029/2022JA030750

Rodger, C. J., Kavanagh, A. J., Clilverd, M. A., & Marple, S. R. (2013). Comparison between POES energetic electron precipitation observations and riometer absorptions: Implications for determining true precipitation fluxes. *Journal of Geophysical Research (Space Physics)*, *118*(12), 7810-7821. doi: 10.1002/2013JA019439

Ross, J. P. J., Glauert, S. A., Horne, R. B., Watt, C. E., Meredith, N. P., & Woodfield, E. E. (2020, October). A New Approach to Constructing Models of Electron Diffusion by EMIC Waves in the Radiation Belts. *Geophysical Res. Lett.*, *47*(20), e88976. doi: 10.1029/2020GL088976

Ross, J. P. J., Glauert, S. A., Horne, R. B., Watt, C. E. J., & Meredith, N. P. (2021, December). On the Variability of EMIC Waves and the Consequences for the Relativistic Electron Radiation Belt Population. *Journal of Geophysical Research (Space Physics)*, *126*(12), e29754. doi: 10.1029/2021JA029754

Sandanger, M. I., Ødegaard, L.-K. G., Nesse Tyssøy, H., Stadsnes, J., Søraas, F., Oksavik, K., & Aarsnes, K. (2015, November). In-flight calibration of NOAA POES proton detectors—Derivation of the MEPED correction factors. *Journal of Geophysical Research (Space Physics)*, *120*(11), 9578-9593. doi: 10.1002/2015JA021388

Selesnick, R. S., Tu, W., Yando, K., Millan, R. M., & Redmon, R. J. (2020). Poes/meped angular response functions and the precipitating radiation belt electron flux. *Journal of Geophysical Research: Space Physics*, *125*(9), e2020JA028240. Retrieved from https://agupubs.onlinelibrary.wiley.com/doi/abs/10.1029/2020JA028240 (e2020JA028240 10.1029/2020JA028240) doi: https://doi.org/10.1029/2020JA028240

Summers, D., & Thorne, R. M. (1991, August). The modified plasma dispersion function. *Physics of Fluids B*, *3*(8), 1835-1847. doi: 10.1063/1.859653

Theodoridis, G. C., & Paolini, F. R. (1967). Pitch angle diffusion of relativistic outer belt electrons. *Ann. Geophys*, *23, 375*.

Tsyganenko, N. A., & Sitnov, M. I. (2005). Modeling the dynamics of the inner magnetosphere during strong geomagnetic storms. *Journal of Geophysical Research: Space Physics*, *110*(A3). Retrieved from `https://agupubs.onlinelibrary.wiley.com/doi/abs/10.1029/2004JA010798` doi: https://doi.org/10.1029/2004JA010798

Watt, C. E. J., Allison, H. J., Meredith, N. P., Thompson, R. L., Bentley, S. N., Rae, I. J., . . . Horne, R. B. (2019, November). Variability of Quasilinear Diffusion Coefficients for Plasmaspheric Hiss. *Journal of Geophysical Research (Space Physics)*, *124*(11), 8488-8506. doi: 10.1029/2018JA026401

Whittaker, I. C., Gamble, R. J., Rodger, C. J., Clilverd, M. A., & Sauvaud, J.-A. (2013). Determining the spectra of radiation belt electron losses: Fitting demeter electron flux observations for typical and storm times. *Journal of Geophysical Research: Space Physics*, *118*(12), 7611-7623. Retrieved from `https://agupubs.onlinelibrary.wiley.com/doi/abs/10.1002/2013JA019228` doi: 10.1002/2013JA019228

Wong, J.-M., Meredith, N. P., Horne, R. B., Glauert, S. A., & Ross, J. P. J. (2022, April). Electron Diffusion by Magnetosonic Waves in the Earth's Radiation Belts. *Journal of Geophysical Research (Space Physics)*, *127*(4), e30196. doi: 10.1029/2021JA030196

Wygant, J. R., Bonnell, J. W., Goetz, K., Ergun, R. E., Mozer, F. S., Bale, S. D., . . . Tao, J. B. (2013, November). The Electric Field and Waves Instruments on the Radiation Belt Storm Probes Mission. *Space Science Review*, *179*(1-4), 183-220. doi: 10.1007/s11214-013-0013-7

Zhao, H., Johnston, W. R., Baker, D. N., Li, X., Ni, B., Jaynes, A. N., . . . Boyd, A. J. (2019, June). Characterization and Evolution of Radiation Belt Electron Energy Spectra Based on the Van Allen Probes Measurements. *Journal of Geophysical Research (Space Physics)*, *124*(6), 4217-4232. doi: 10.1029/2019JA026697

Acknowledgments

This work was supported by NERC Highlight Topic Grant NE/P01738X/1 (Rad-Sat) and NERC National Capability grants NE/R016038/1 and NE/R016445/1. We thank Janet Green for her bow tie analysis software of the POES data. We also thanks the Polar Data Centre for their help with preparing the data for publication.

Figure 1.

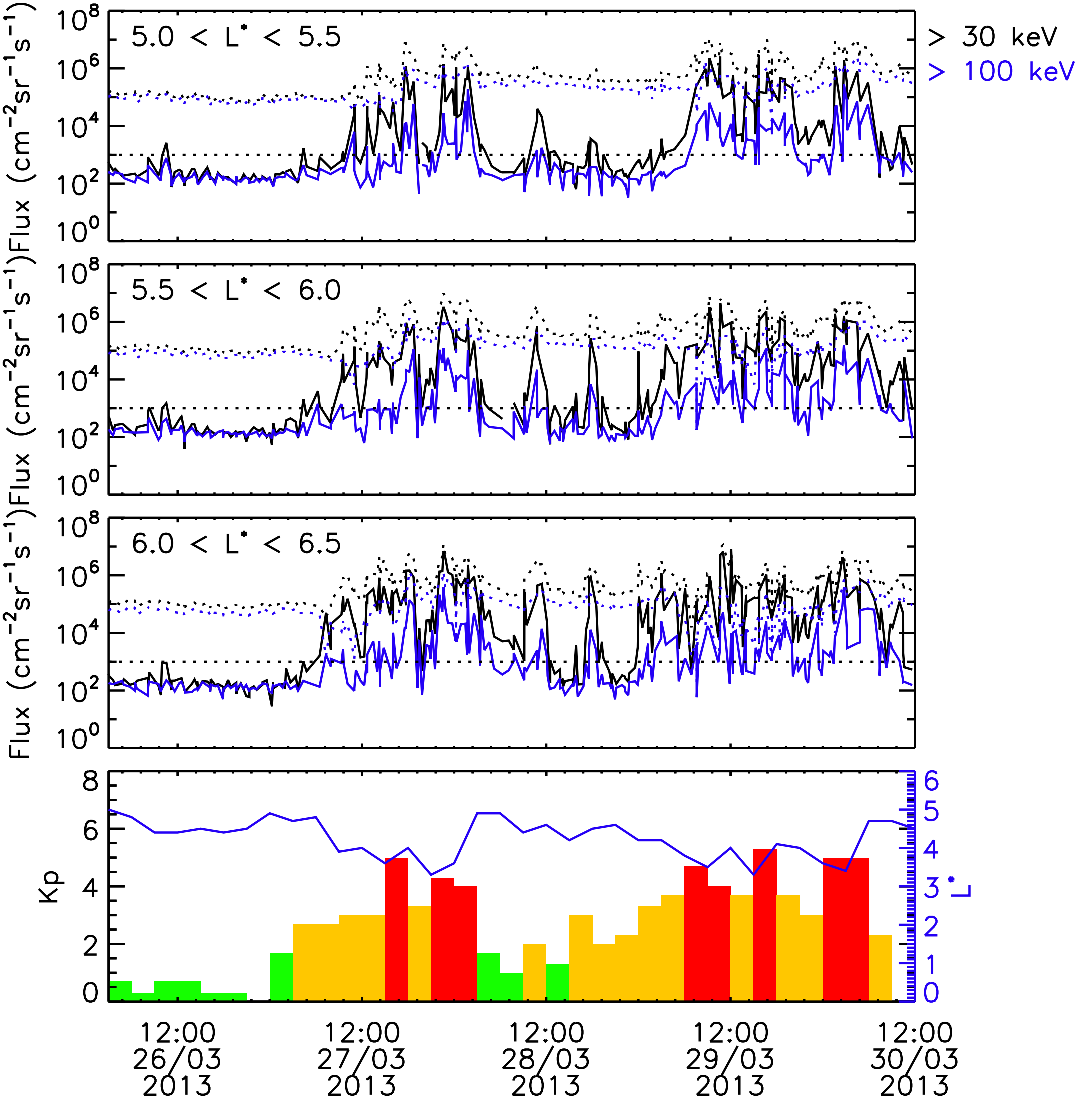

5.0 < L* < 5.5
5.5 < L* < 6.0
6.0 < L* < 6.5
> 30 keV
> 100 keV
Flux (cm^-2 sr^-1 s^-1)
Kp
L*
12:00 26/03 2013
12:00 27/03 2013
12:00 28/03 2013
12:00 29/03 2013
12:00 30/03 2013

Figure 2.

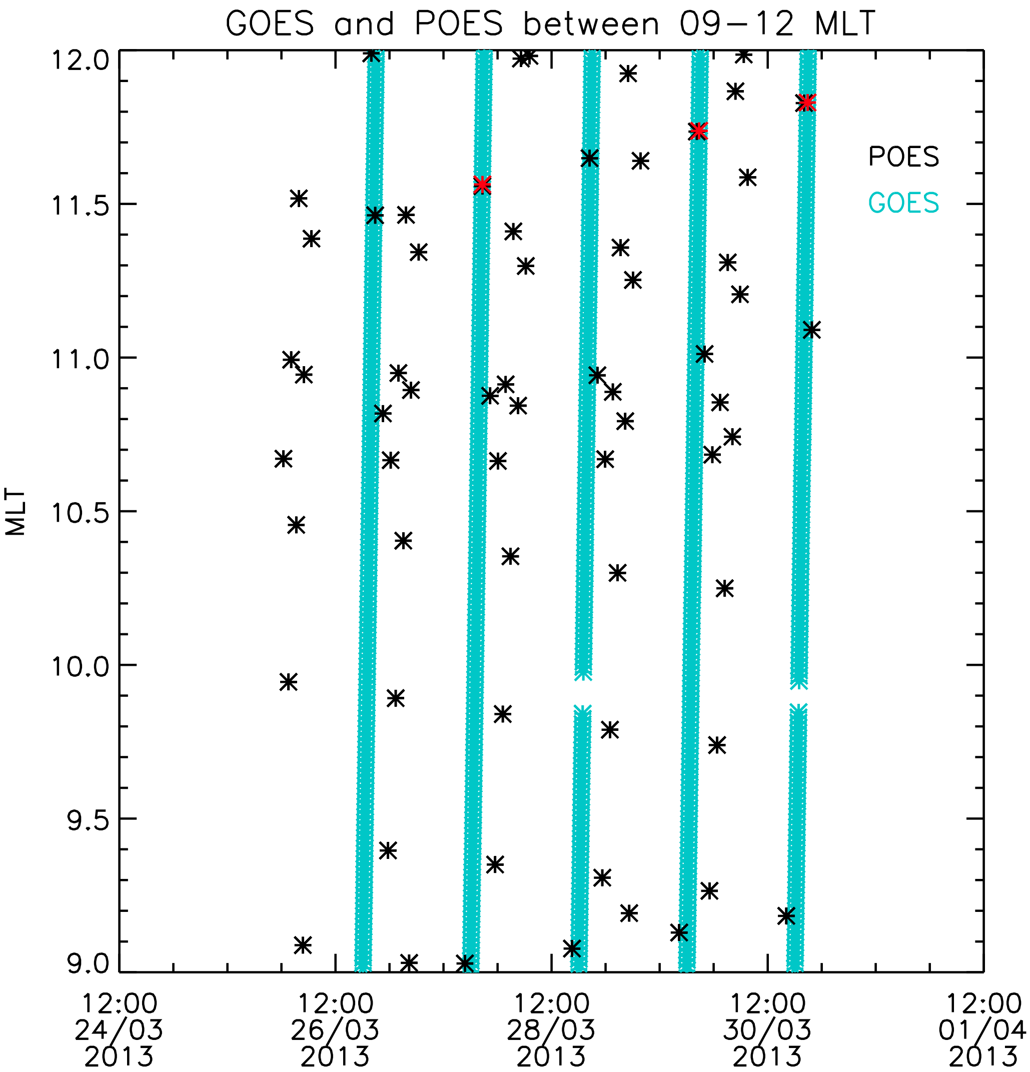

GOES and POES between 09–12 MLT
MLT
12.0
11.5
11.0
10.5
10.0
9.5
9.0
POES
GOES
12:00 24/03 2013
12:00 26/03 2013
12:00 28/03 2013
12:00 30/03 2013
12:00 01/04 2013

Figure 3.

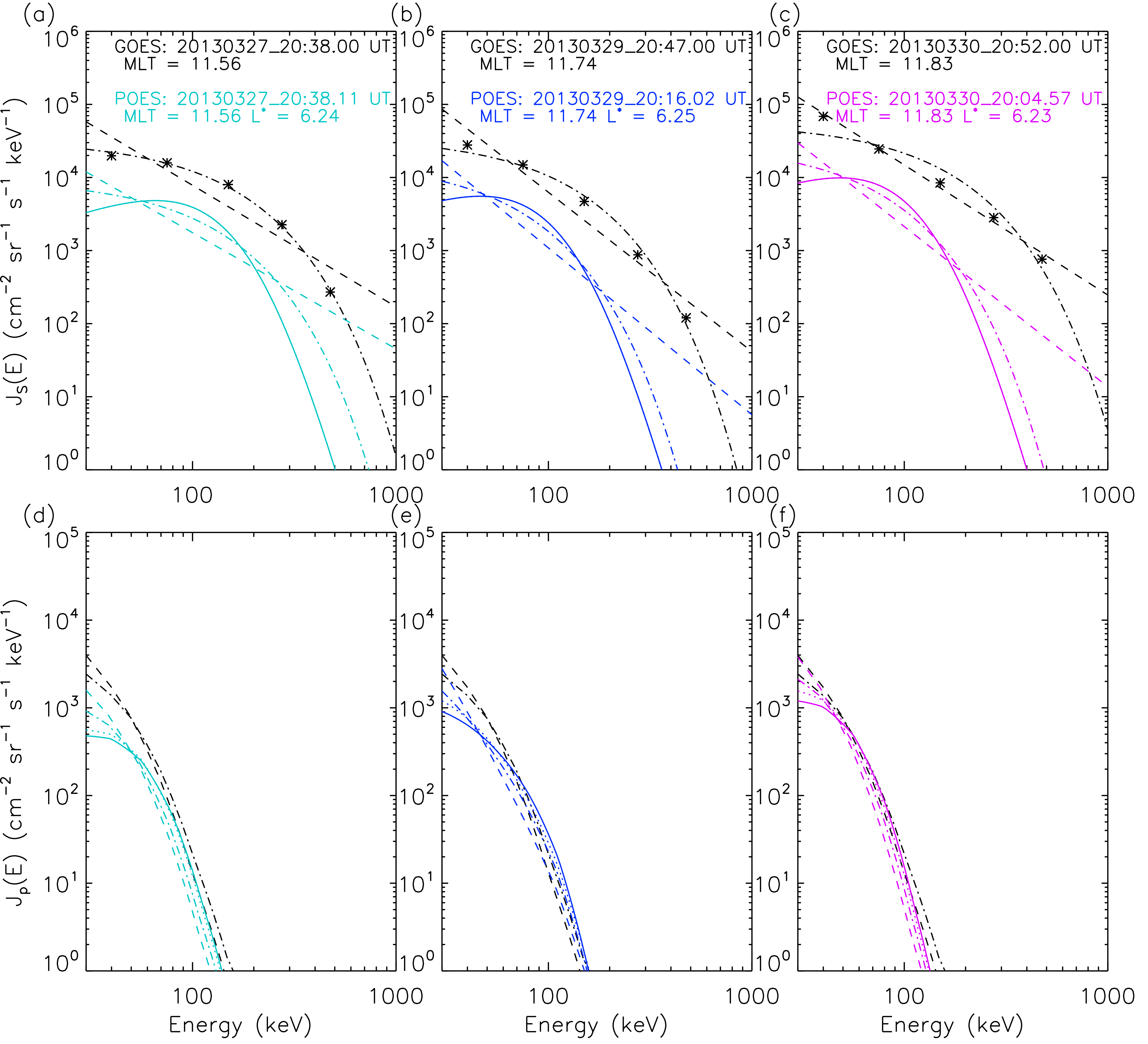
(a)
GOES: 20130327_20:38.00 UT
MLT = 11.56
POES: 20130327_20:38.11 UT
MLT = 11.56 L* = 6.24
(b)
GOES: 20130329_20:47.00 UT
MLT = 11.74
POES: 20130329_20:16.02 UT
MLT = 11.74 L* = 6.25
(c)
GOES: 20130330_20:52.00 UT
MLT = 11.83
POES: 20130330_20:04.57 UT
MLT = 11.83 L* = 6.23
(d)
(e)
(f)
J_S(E) (cm^-2 sr^-1 s^-1 keV^-1)
J_p(E) (cm^-2 sr^-1 s^-1 keV^-1)
Energy (keV)

Figure 4.

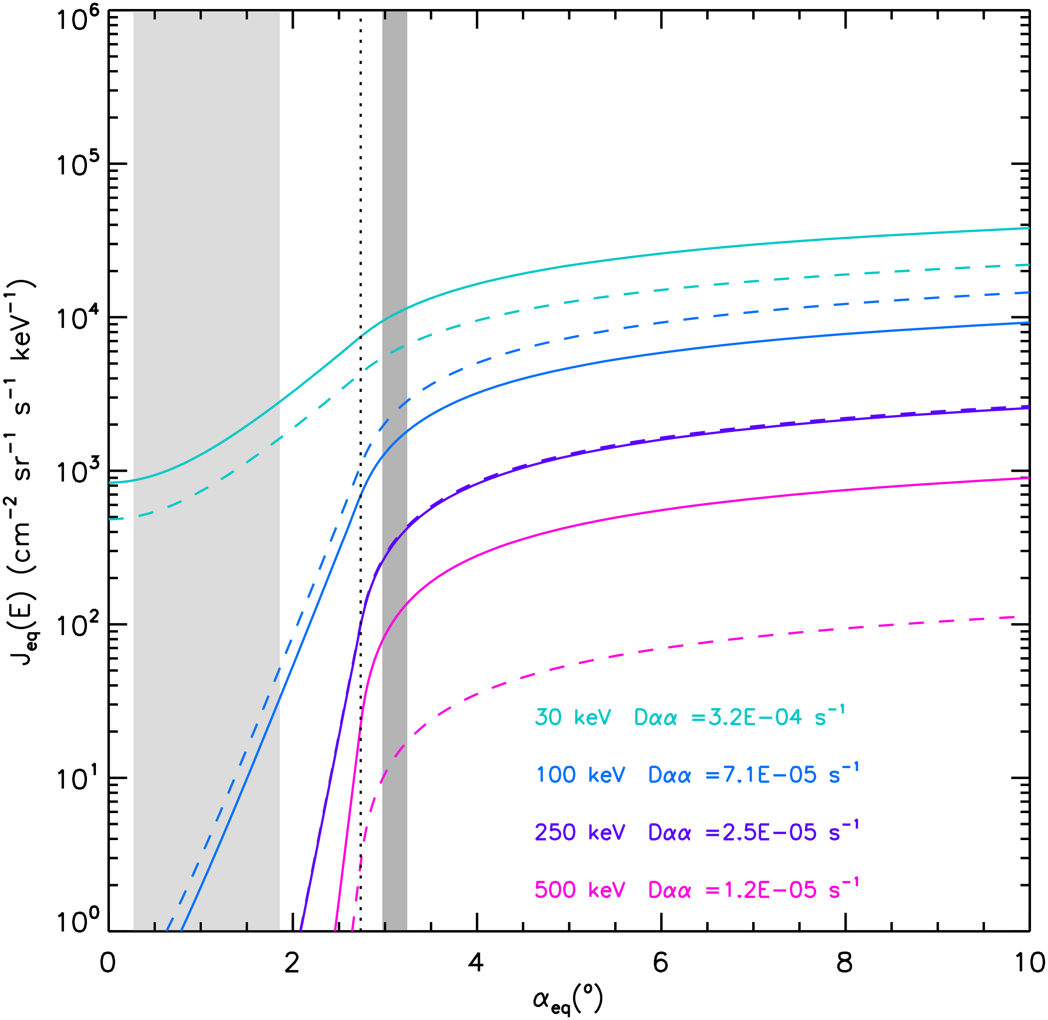

10^6
10^5
10^4
10^3
10^2
10^1
10^0
$J_{eq}(E)$ $(cm^{-2}\ sr^{-1}\ s^{-1}\ keV^{-1})$
0
2
4
6
8
10
$\alpha_{eq}(^o)$
30 keV $D\alpha\alpha$ =3.2E-04 s^{-1}
100 keV $D\alpha\alpha$ =7.1E-05 s^{-1}
250 keV $D\alpha\alpha$ =2.5E-05 s^{-1}
500 keV $D\alpha\alpha$ =1.2E-05 s^{-1}

Figure 5.

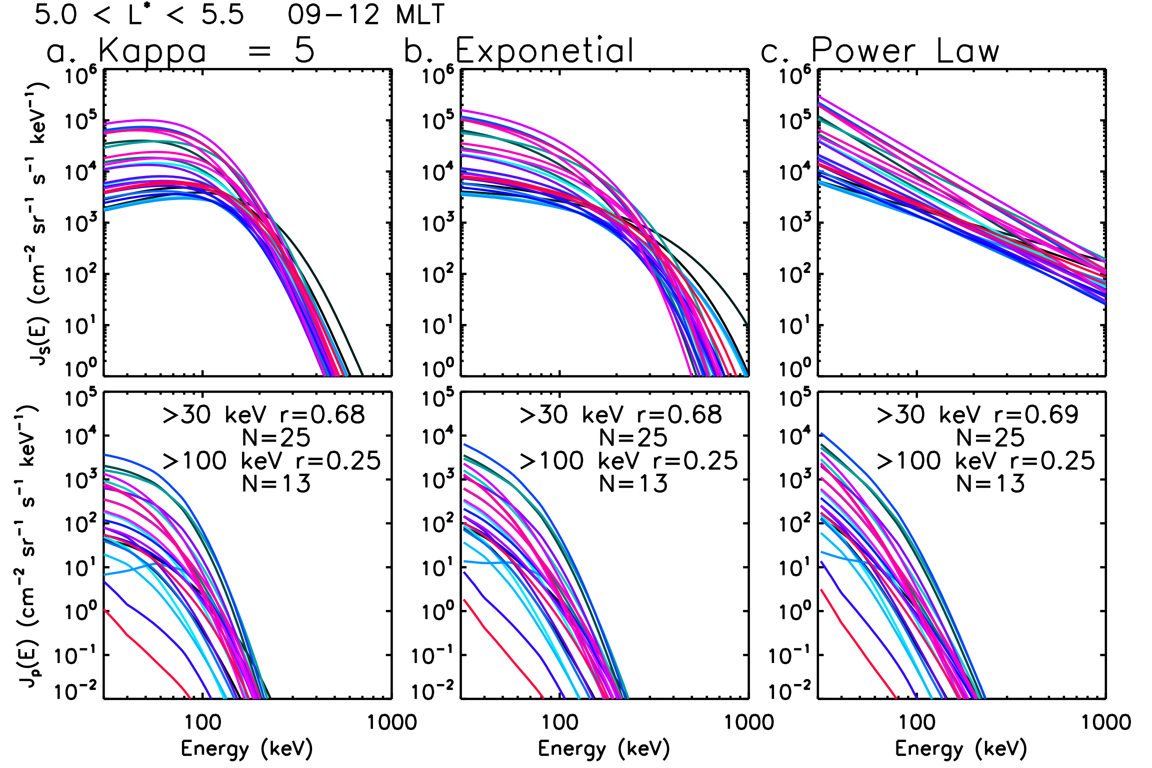

5.0 < L* < 5.5 09–12 MLT
a. Kappa = 5
b. Exponetial
c. Power Law
J_S(E) (cm^-2 sr^-1 s^-1 keV^-1)
J_P(E) (cm^-2 sr^-1 s^-1 keV^-1)
>30 keV r=0.68
N=25
>100 keV r=0.25
N=13
>30 keV r=0.68
N=25
>100 keV r=0.25
N=13
>30 keV r=0.69
N=25
>100 keV r=0.25
N=13
Energy (keV)
Energy (keV)
Energy (keV)

Figure 6.

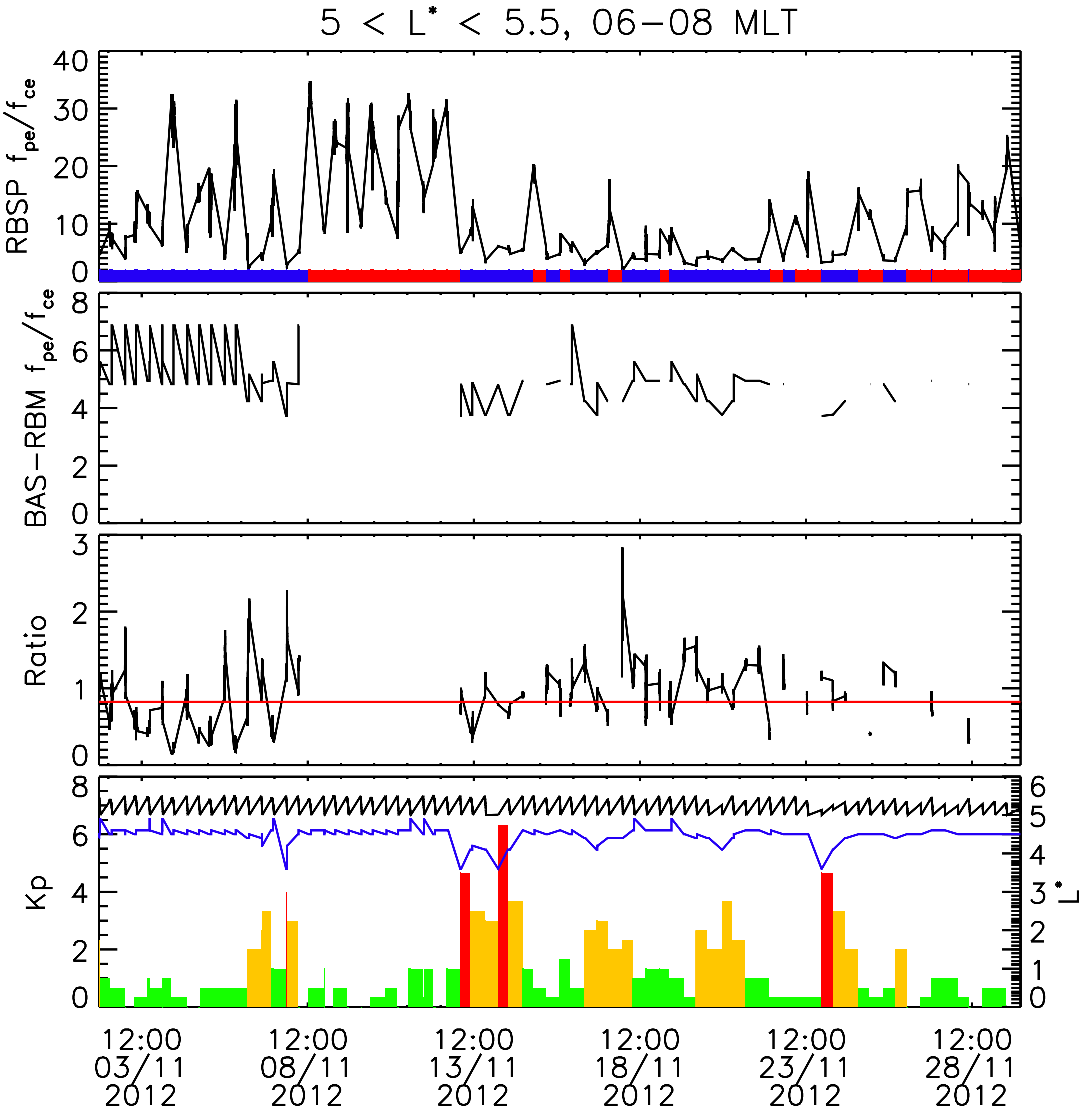

5 < L* < 5.5, 06–08 MLT
RBSP f_pe/f_ce
BAS–RBM f_pe/f_ce
Ratio
Kp
L*
0
10
20
30
40
0
2
4
6
8
0
1
2
3
0
2
4
6
8
0
1
2
3
4
5
6
12:00
03/11
2012
12:00
08/11
2012
12:00
13/11
2012
12:00
18/11
2012
12:00
23/11
2012
12:00
28/11
2012

Figure 7.

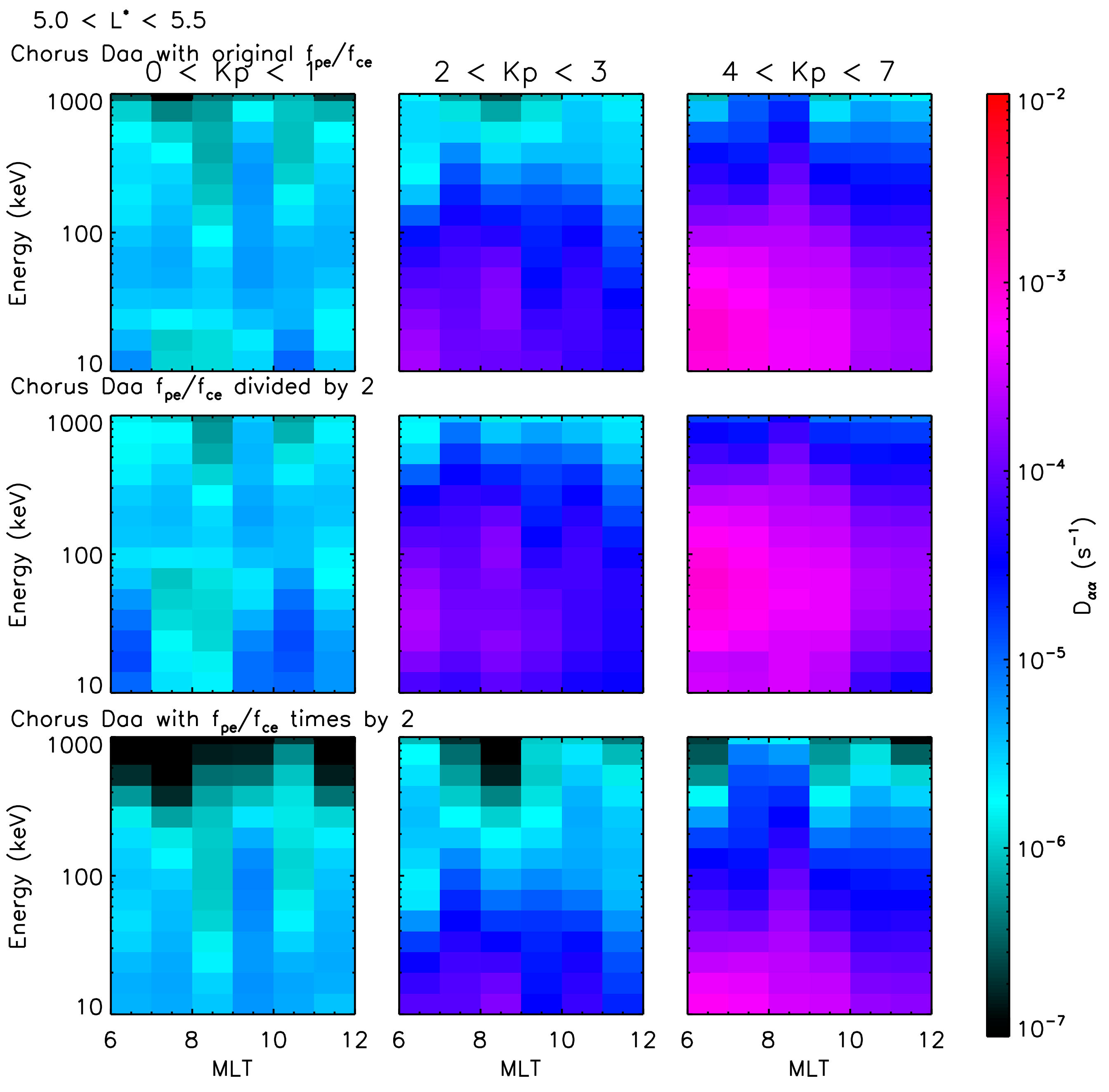

5.0 < L* < 5.5
Chorus Daa with original f_{pe}/f_{ce}
0 < Kp < 1
2 < Kp < 3
4 < Kp < 7
Chorus Daa f_{pe}/f_{ce} divided by 2
Chorus Daa with f_{pe}/f_{ce} times by 2
Energy (keV)
1000
100
10
MLT
6
8
10
12
$D_{\alpha\alpha}$ (s^{-1})
10^{-2}
10^{-3}
10^{-4}
10^{-5}
10^{-6}
10^{-7}

Figure 8.

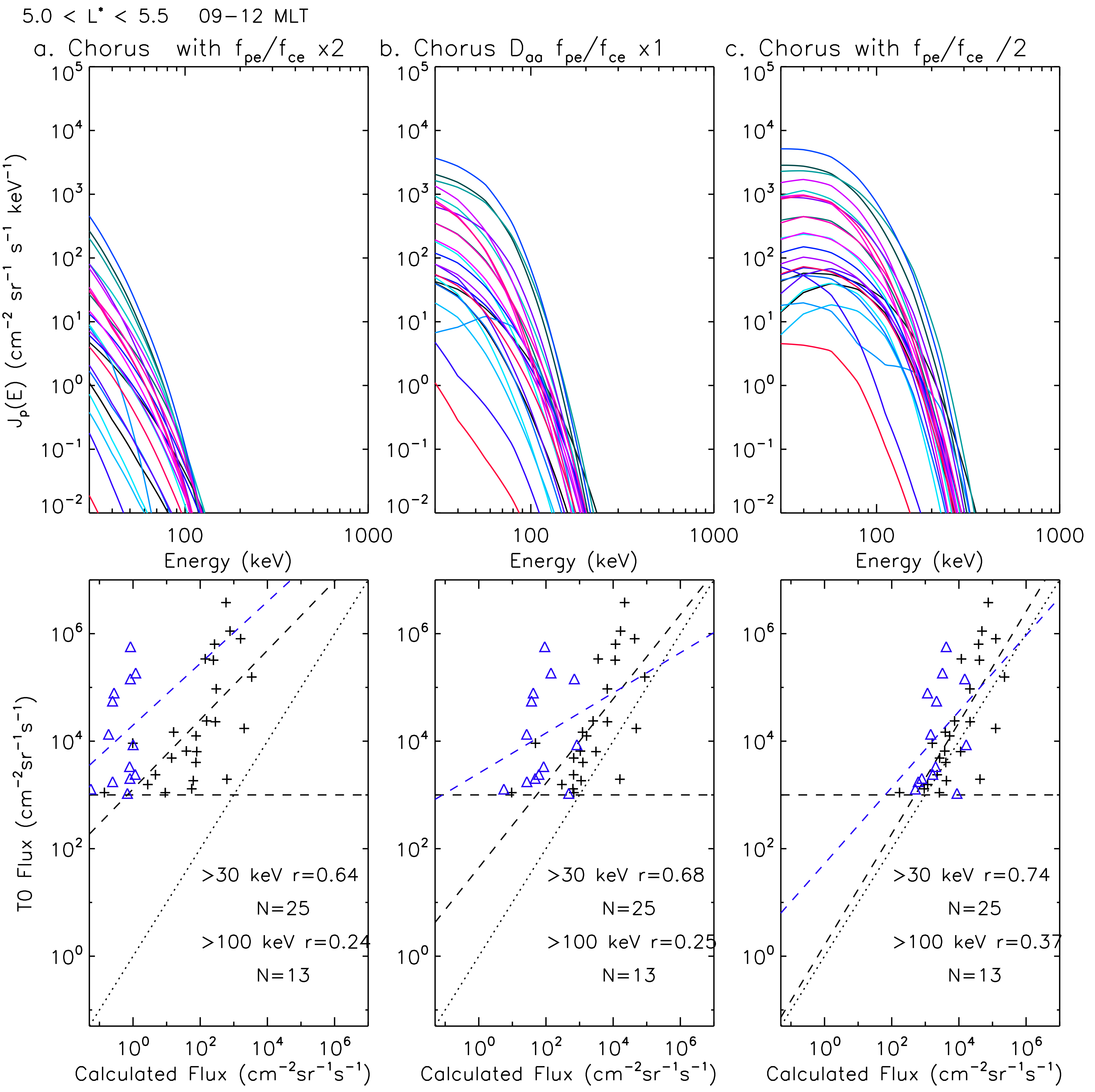

5.0 < L* < 5.5 09-12 MLT
a. Chorus with fpe/fce x2
b. Chorus Daa fpe/fce x1
c. Chorus with fpe/fce /2
Jp(E) (cm-2 sr-1 s-1 keV-1)
Energy (keV)
T0 Flux (cm-2sr-1s-1)
Calculated Flux (cm-2sr-1s-1)
>30 keV r=0.64
N=25
>100 keV r=0.24
N=13
>30 keV r=0.68
N=25
>100 keV r=0.25
N=13
>30 keV r=0.74
N=25
>100 keV r=0.37
N=13

Figure 9.

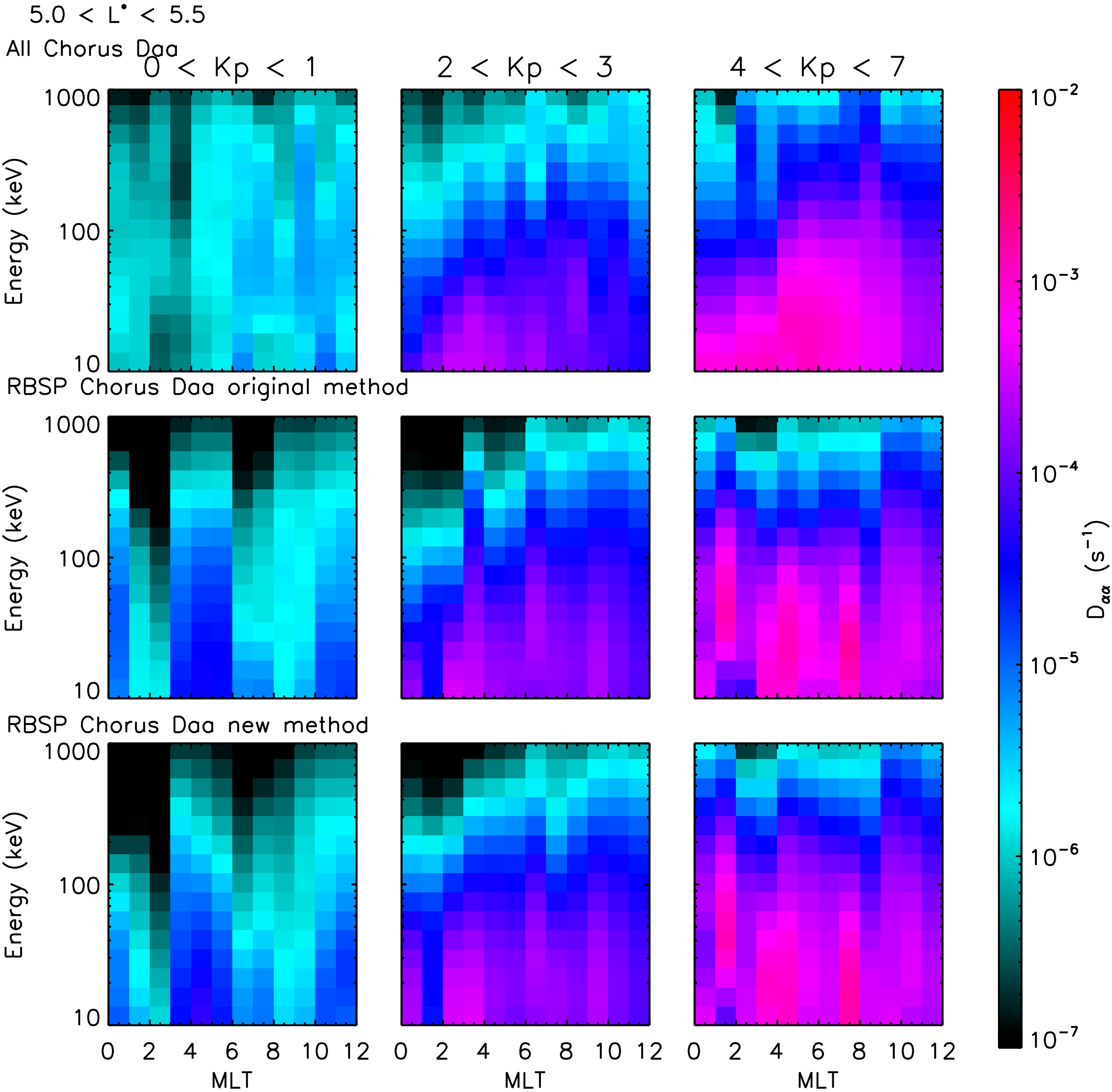

5.0 < L* < 5.5
All Chorus Daa
0 < Kp < 1
2 < Kp < 3
4 < Kp < 7
RBSP Chorus Daa original method
RBSP Chorus Daa new method
Energy (keV)
1000
100
10
MLT
0 2 4 6 8 10 12
$D_{\alpha\alpha}$ (s^{-1})
10^{-2}
10^{-3}
10^{-4}
10^{-5}
10^{-6}
10^{-7}

Figure 10.

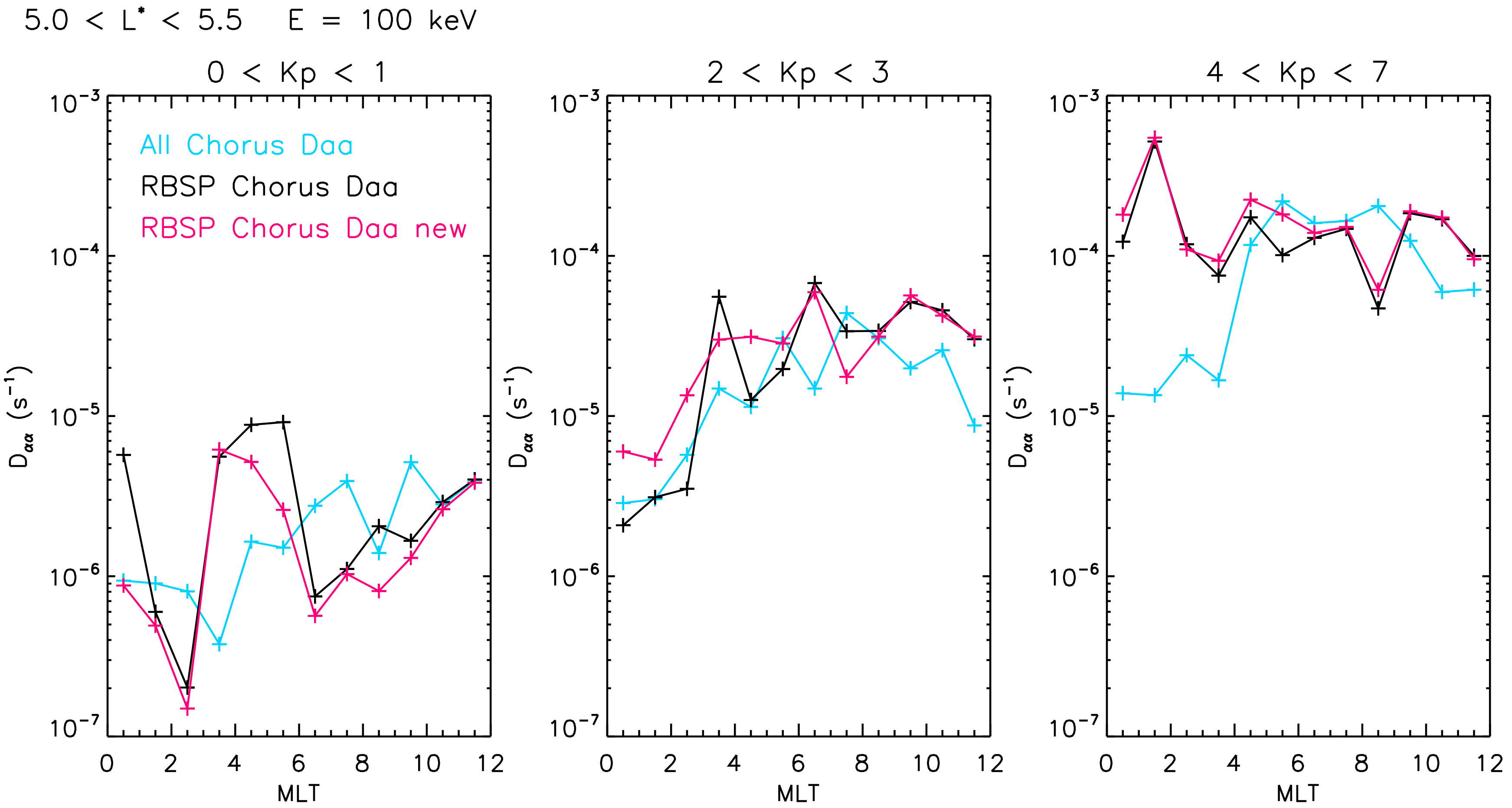
5.0 < L* < 5.5 E = 100 keV
0 < Kp < 1
2 < Kp < 3
4 < Kp < 7
All Chorus Daa
RBSP Chorus Daa
RBSP Chorus Daa new
$D_{\alpha\alpha}$ (s^{-1})
MLT

Figure 11.

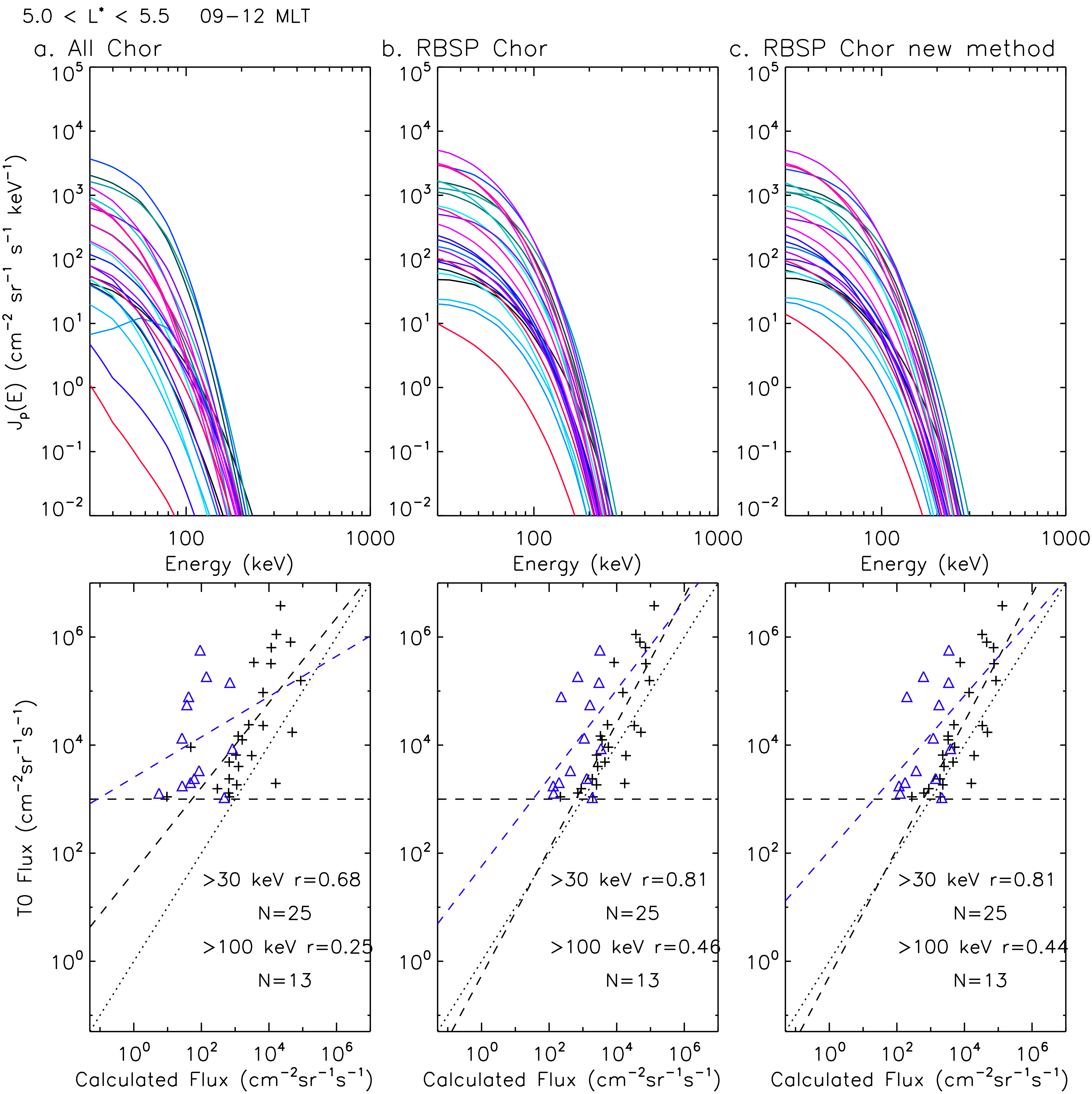

5.0 < L* < 5.5 09–12 MLT
a. All Chor
b. RBSP Chor
c. RBSP Chor new method
J_p(E) (cm^-2 sr^-1 s^-1 keV^-1)
Energy (keV)
T0 Flux (cm^-2sr^-1s^-1)
Calculated Flux (cm^-2sr^-1s^-1)
>30 keV r=0.68
N=25
>100 keV r=0.25
N=13
>30 keV r=0.81
N=25
>100 keV r=0.46
N=13
>30 keV r=0.81
N=25
>100 keV r=0.44
N=13

Figure 12.

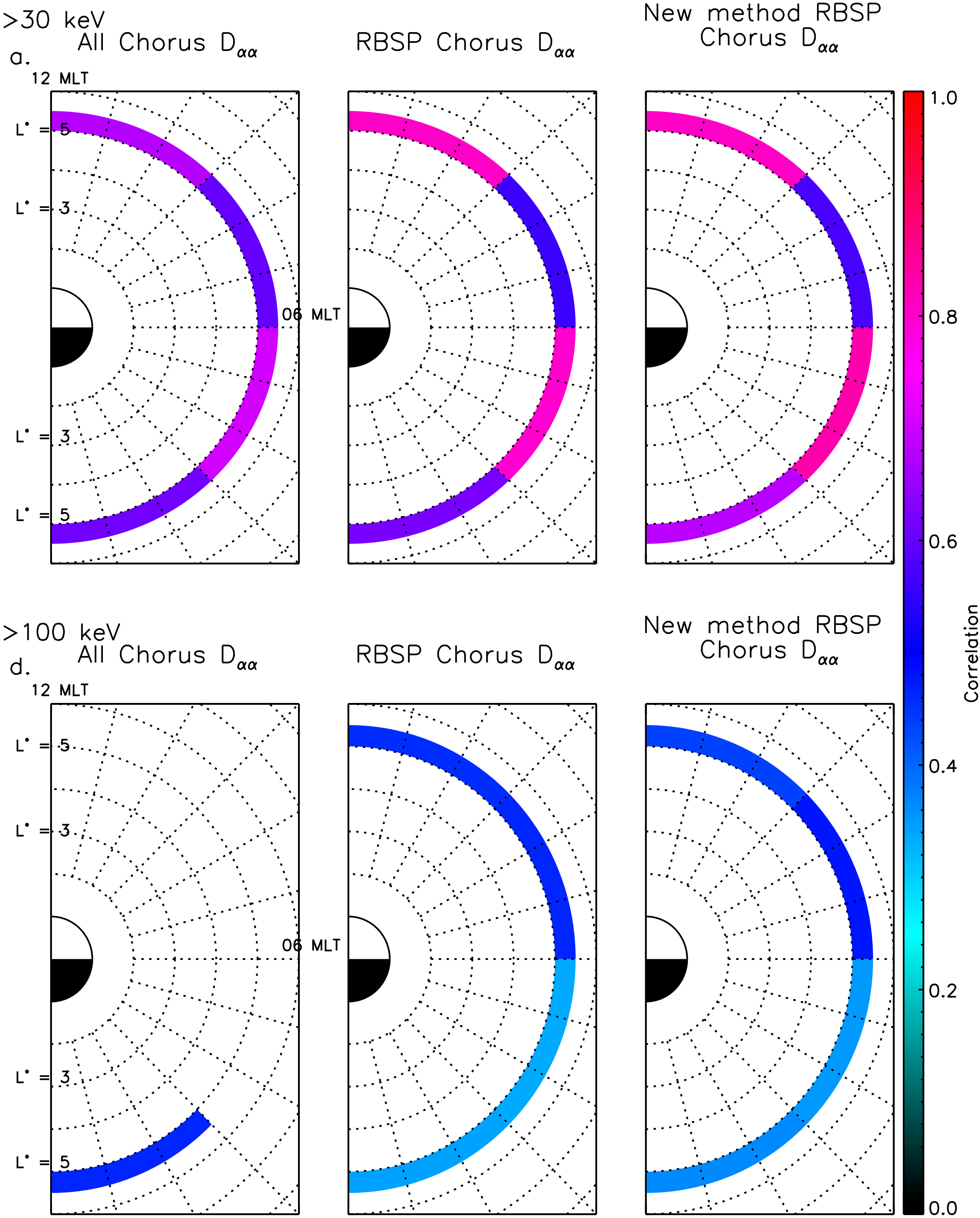

>30 keV
a.
All Chorus $D_{\alpha\alpha}$
RBSP Chorus $D_{\alpha\alpha}$
New method RBSP Chorus $D_{\alpha\alpha}$
12 MLT
L* = 5
L* = 3
06 MLT
L* = 3
L* = 5
>100 keV
d.
All Chorus $D_{\alpha\alpha}$
RBSP Chorus $D_{\alpha\alpha}$
New method RBSP Chorus $D_{\alpha\alpha}$
12 MLT
L* = 5
L* = 3
06 MLT
L* = 3
L* = 5
1.0
0.8
0.6
0.4
0.2
0.0
Correlation

Figure 13.

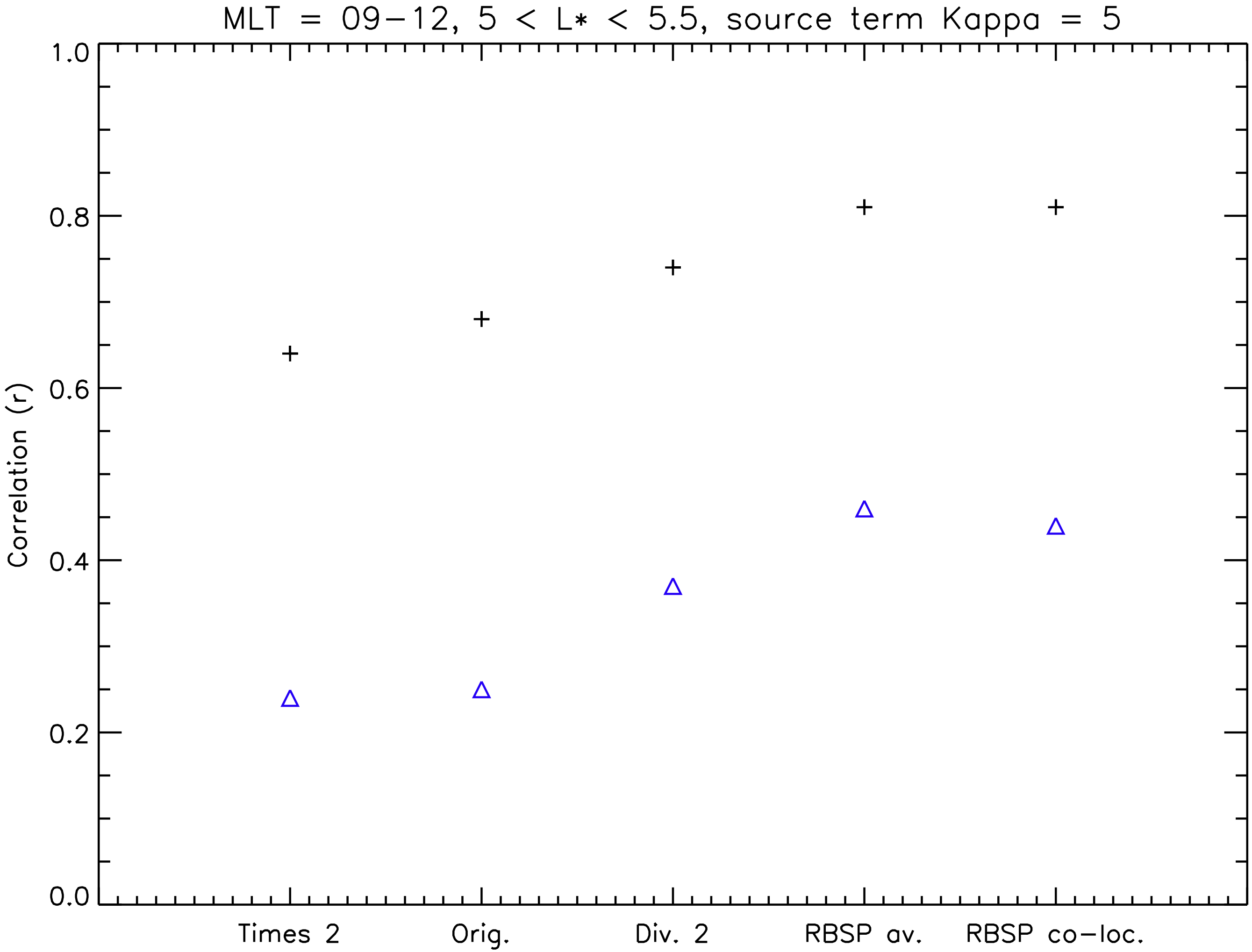

MLT = 09−12, 5 < L* < 5.5, source term Kappa = 5
Correlation (r)
1.0
0.8
0.6
0.4
0.2
0.0
Times 2
Orig.
Div. 2
RBSP av.
RBSP co−loc.